

MOL # 116871

*1. Title page*

Mutational analysis and modeling of negative allosteric modulator binding sites in AMPA receptors

Charlotte Stenum-Berg, Maria Musgaard, Sergei Chavez-Abiega, Christine L. Thisted, Lorenzo Barrella, Philip C. Biggin, Anders S. Kristensen

Department of Drug Design and Pharmacology, University of Copenhagen, Universitetsparken 2, DK-2100 Copenhagen, Denmark

(CSB, SCA, CLT, LB, ASK)

Department of Biochemistry, University of Oxford, Oxford, United Kingdom

(MM, PCB)

Present address: Department of Chemistry and Biomolecular Sciences, University of Ottawa, Ottawa, Canada

(MM)

MOL # 116871

## 2. Running title page

### *Running title:*

Binding of negative allosteric modulators in AMPA receptors

### *Corresponding author information:*

Anders S. Kristensen, Department of Drug Design and Pharmacology, University of Copenhagen, Universitetsparken 2, DK-2100 Copenhagen, Denmark. E-mail: ask@sund.ku.dk. Tel.: +45 35 33 65 05

*Text pages:* 24

*Tables:* 2

*Figures:* 9

*References:* 55

*Abstract:* 250 words

*Introduction:* 748 words

*Discussion:* 1403 words

### *Abbreviations:*

AMPA:  $\alpha$ -Amino-3-hydroxy-5-methyl-4-isoxazolepropionic acid

AMPA: AMPA receptor

ATD: Amino-terminal domain

*blac*:  $\beta$ -lactamase

CP: CP-465,022

CNQX: 6-cyano-7-nitroquinoxaline-2,3-dione

CNS: Central nervous system

CTD: Carboxy-terminal domain

CTZ: Cyclothiazide

DMEM: Dulbecco's modified Eagle's medium

EPSC: Excitatory post-synaptic current

GYKI: GYKI-53,655

iGluR: Ionotropic glutamate receptor

LBD: Ligand-binding domain

LTD: Long-term depression

LTP: Long-term potentiation

NAM: Negative allosteric modulator

**MOL # 116871**

PAM: Positive allosteric modulators

PBSCM: Phosphate buffered saline supplemented with CaCl<sub>2</sub> and MgCl<sub>2</sub>

PMP: Perampanel

TEVC: Two-electrode voltage clamp

TMD: Transmembrane domain

WT: Wild-type

### 3. Abstract

The  $\alpha$ -Amino-3-hydroxy-5-methyl-4-isoxazolepropionic acid receptors (AMPA<sub>R</sub>s) constitute a subclass of the ionotropic glutamate receptor (iGlu<sub>R</sub>) superfamily, which functions as glutamate-gated cation channels to mediate the majority of excitatory neurotransmission in the central nervous system (CNS). AMPA<sub>R</sub>s are therapeutic targets in a range of brain disorders associated with abnormal glutamate hyperactivity. Multiple classes of AMPA<sub>R</sub> inhibitors have been developed during the past decades, including competitive antagonists, ion channel blockers and negative allosteric modulators (NAMs). At present, NAMs is the only class of AMPA<sub>R</sub> ligands that have been developed into safe and useful drugs in humans in the form of perampanel (Fycompa), which was recently approved for treatment of epilepsy. Compared to the detailed understanding of other AMPA<sub>R</sub> ligand classes, surprisingly little information has been available regarding the molecular mechanism of perampanel and other classes of NAMs at AMPA<sub>R</sub>s; including the location and structure of NAM binding pockets in the receptor complex. However, structures of the AMPA<sub>R</sub> GluA2 in complex with NAMs were recently reported that unambiguously identified the NAM binding sites. In parallel with this work, our aim with the present study was to identify specific residues involved in the formation of the NAM binding site for three prototypical AMPA<sub>R</sub> NAMs. Hence, we have performed a mutational analysis of the AMPA<sub>R</sub> region that links the four extracellular ligand-binding domains (LBDs) to the central ion channel in the transmembrane domain (TMD) region. We furthermore perform computational ligand-docking of the NAMs into structural models of the homomeric GluA2 receptor and optimize side chain conformations around the NAMs to model how NAMs bind in this specific site. The new insights provide potentially valuable input for structure-based drug design of new NAMs.

MOL # 116871

#### ***4. Significance statement***

AMPA receptors are glutamate-gated ion channels that mediate the majority of excitatory neurotransmission in the brain. Negative allosteric modulators (NAMs) of AMPA receptors are considered to have significant therapeutic potential in diseases linked to glutamate hyperactivity. The present work employs mutational analysis and molecular modeling of the binding site for prototypical NAMs to provide new molecular insight into how NAMs interact with the AMPA receptor, which is of potential use for future design of new types of NAMs.

## 5. Introduction

AMPA receptors (AMPA-Rs) mediate the majority of excitatory post-synaptic currents (EPSCs) in the CNS (Traynelis et al., 2010) by utilizing energy from the binding of glutamate (Glu) to drive ion channel opening. In addition to a central role in basal excitatory neurotransmission, AMPARs are involved in synaptic plasticity mechanisms such as long-term potentiation (LTP) and long-term depression (LTD) that underlie learning and memory (Kessels and Malinow, 2009). AMPARs assemble as tetramers from combinations of GluA1-GluA4 subunits as well as a range of auxiliary subunits of different classes that can modulate receptor function (Haering et al., 2014; Jackson and Nicoll, 2011); generating a range of subtypes with overall similar core function, but with differences in biophysical properties, pharmacology, and regulatory mechanisms (Cokic and Stein, 2008; Jackson and Nicoll, 2011). Structures are currently available of homomeric and heteromeric AMPARs in resting (Herguedas et al., 2019; Sobolevsky et al., 2009; Zhao et al., 2019), active (Chen et al., 2017; Twomey et al., 2017a), and desensitized (Chen et al., 2017; Twomey et al., 2017b) states. These have advanced the molecular understanding of AMPARs by providing insight to the structural mechanisms underlying receptor function and pharmacology (Karakas et al., 2015; Kumar and Mayer, 2013; Twomey and Sobolevsky, 2018; Zhu and Gouaux, 2017).

Abnormal AMPAR activity is involved in neurological diseases, and compounds that can modify AMPAR signaling has for decades been pursued as potential therapeutics in treatment of Alzheimer's disease, Parkinson's disease, depression and epilepsy (Citraro et al., 2014; Di Bonaventura et al., 2017; Traynelis et al., 2010; Zarate and Manji, 2008). AMPARs contain multiple binding sites where small-molecule ligands can modulate receptor function positively or negatively via allosteric effects on core channel function (Karakas et al., 2015; Traynelis et al., 2010). This includes NAMs, which bind outside the orthosteric binding site or the ion channel and inhibit the receptor by non-competitive mechanisms. Several chemical classes of AMPAR NAMs are known and include 2,3-benzodiazepines (Solyom and Tarnawa, 2002), quinazolinones (Lazzaro et al., 2002), and pyridones (Zwart et al., 2014). Among these, the pyridone-based perampanel (PMP) under the trade name Fycompa was recently approved as a first-in-class AMPAR drug for treatment of epilepsy (Hanada, 2014), thereby demonstrating the potential of negative allosteric modulation of AMPARs in treatment of neurological diseases linked to glutamatergic hyperfunction (Di Bonaventura et al., 2017). However, the molecular mechanisms underlying NAM inhibition of AMPARs are surprisingly poorly understood for all NAM classes; including the location and structure of the NAM binding pockets and how ligand binding can inhibit channel gating.

The AMPAR structure is highly modular and contains extracellular amino-terminal and ligand-binding domains (ATD and LBD, respectively), a transmembrane domain (TMD) with the ion channel, and a cytoplasmic carboxyl-terminal domain (CTD) (Kumar and Mayer, 2013; Sobolevsky et al., 2009). Channel gating involves allosteric coupling between LBD motions and the TMD via short flexible linkers. Binding

**MOL # 116871**

studies have indicated that NAMs of the 2,3-benzodiazepine, quinazolinone, and pyridone class share the same binding site (Menniti et al., 2000; Micale et al., 2008; Mittapalli and Roberts, 2014; Solyom and Tarnawa, 2002), which is distinct from the well-characterized binding sites for positive allosteric modulators at the LBD interfaces (Sun et al., 2002). Early work suggested that NAM binding sites were located in the LBD-TMD linker region and identified residues in the linkers connecting the S1-M1 and S2-M4 regions to affect NAM inhibitory potency (Balannik et al., 2005; Cokic and Stein, 2008). Now, structures of homomeric GluA2 in complex with NAMs are available that unambiguously identified that each subunit contains a NAM binding pocket formed between the upper M3 transmembrane helix and the S1-M1 and S2-M4 linkers (Yelshanskaya et al., 2016). Although these structures contained electron densities for the bound NAM ligands, the resolution of approximately 4 Å did not allow direct identification of NAM-protein interactions (Twomey and Sobolevsky, 2018).

We have conducted a mutational analysis of the LBD-TMD linker regions in the GluA2 subunit to further study the role LBD-TMD linker residues for the function of three prototypical NAMs in the form of PMP, the 2,3-benzodiazepine GYKI-53,655 (GYKI) (Moncada et al., 1991), and the quinazolinone CP-465,022 (CP) (Menniti et al., 2000). Our initial aim was to use the resulting data set to specify the location of NAM binding pockets in the linker region and use computational ligand-docking of NAMs into GluA2 structures to create binding mode models. We used the new GluA2/NAM structures as templates to create binding models that include all side chains. In combination with our mutational analysis, the models provide molecular insight into ligand orientations and specific protein-ligand contacts for the investigated NAMs.

## 6. Materials and Methods

**Materials** – All chemicals were from Sigma-Aldrich (St. Louis, MO) unless otherwise stated. Dulbecco's modified Eagle's medium (DMEM), fetal bovine serum, trypsin, and penicillin-streptomycin were from Invitrogen (Carlsbad, CA). DNA modifying enzymes were from New England Biolabs (Ipswich, MA) except PfuUltra II Fusion HS DNA polymerase (Agilent, Carlsbad, CA) and Rapid T4 ligase (Roche Molecular Systems, Pleasanton, CA). All tissue cell culture plastic ware was from Sarstedt (Nümbrecht, Germany) unless otherwise stated. 6-cyano-7-nitroquinoxaline-2,3-dione (CNQX), cyclothiazide (CTZ), and CP-465,022 hydrochloride were from HelloBio (Bristol, UK). GYKI-53,655 or GYKI-53,655 hydrochloride was from Axon MedChem (Groningen, Netherlands) or Tocris Bioscience (Bristol, UK). Perampanel was from Toronto Research Chemicals (Toronto, Ontario, Canada) or Apexmol (Beijing, China). The calcium dyes Fluo-2 or Fluo-8 AM were from TEF Labs (Austin, TX) or AAT Bioquest (Sunnyvale, CA).

**Molecular Biology** – The plasmid vectors pRK5 (BD PharMingen, San Diego, USA), pGEM-HE (Liman et al., 1992) and pXOOF containing cDNA for the unedited flip isoform of rat GluA2 gene were used for expression in mammalian cells or generation of mRNA for microinjection in *Xenopus laevis* oocytes. The pXOOF vector is a modified version of the dual-purpose mammalian and *Xenopus* expression vector pXOON (Jespersen et al., 2002) in which cDNA encoding enhanced green fluorescent protein (eGFP) is removed. Specifically, we created pXOOF by PCR amplification of the entire pXOON sequence excluding the eGFP gene using forward and reverse PCR primers with 5' overhang recognition sequence for the restriction enzyme *SbfI*. The resulting linear DNA fragment was *SbfI* digested and re-ligated using T4 DNA ligase (Roche, Mannheim, Germany) to generate pXOOF. The pXOOF plasmid sequence was verified by DNA sequencing. Generation of GluA2 point-mutants was performed by site-directed mutagenesis using the QuickChange mutagenesis kit (Stratagene, La Jolla, CA). The mutations were verified by DNA sequencing of the entire GluA2 gene (GATC Biotech, Constance, Germany). For analysis of cell-surface expression of wild-type (WT) and mutant GluA2 receptors, cDNA encoding  $\beta$ -lactamase (*blac*) were inserted in the GluA2 cDNA in between the segments encoding the N-terminal signal sequence and the ATD. Specifically, using In-Fusion cloning (Mountain View, CA, USA), a PCR-amplified DNA fragment encoding *blac* flanked by two short amino acid linkers (GGSGS and GGSG) was inserted in-frame into an *AfeI* site introduced by site-directed mutagenesis of codon 26 and 27 in the GluA2 sequence to create *blac*-GluA2. For use as template for *in vitro* transcription of cRNA, pGEM-HE and pXOOF plasmid constructs were linearized downstream of the 3' untranslated region of the *Xenopus*  $\beta$ -globin sequence using *NheI*-HF restriction enzyme, and purified by ethanol precipitation with Pellet Paint NF Co-Precipitant (Merck, Billerica, MA, USA). cRNA transcription was performed using the AmpliCap-Max T7 High Yield Message Maker Kit (CellScript, Madison, WI, USA) and cRNA was column purified using NucleoSpin RNA Clean-up XS kit (Macherey-Nagel; Düren, Germany).

**MOL # 116871**

*Mammalian Cell Culturing and Expression* – HEK293T cells (American Type Culture Collection, Manassas, VA) were cultured in growth medium (DMEM supplemented with 10% v/v fetal bovine serum, 100 units/ml penicillin, and 100 µg/ml streptomycin) at 37 °C in a humidified 5% CO<sub>2</sub> environment. For expression of WT and mutant GluA2 in HEK293 cells, TransIT-LT1 DNA transfection reagent (Mirus, Madison, WI) was used as described previously (Sorensen et al., 2014). Briefly, HEK293 cells in suspension (1e6 cells/mL) were mixed with DNA/transfection complex (formed by mixing plasmid DNA, TransIT-LT1 reagent and DMEM in a 1:3:90 ratio) and plated into poly-D-lysine coated Falcon® black clear-bottom 96-well plates (Corning, Corning, NY, USA) to a final density of approximately 20,000 cells and 0.1 µg plasmid DNA per well. The competitive antagonist CNQX was added at a final concentration of 20 µM to protect against glutamate-induced cytotoxicity in the transfected cultures. Cells were incubated for two days after transfection before experiments.

*Xenopus Laevis Oocyte Expression* – Defolliculated *Xenopus* oocytes (stage V to VI) were prepared and injected with 1 to 25 ng mRNA, as described previously (Poulsen et al., 2013). The care and use of *Xenopus laevis* were in strict adherence to a protocol (license 2014–15–0201–00031) approved by the Danish Veterinary and Food Administration. Injected oocytes were incubated at 18 °C in Standard Barth's Solution (SBS) containing (in mM) 88 NaCl, 1 KCl, 0.41 CaCl<sub>2</sub>, 2.4 NaHCO<sub>3</sub>, 0.33 Ca(NO<sub>3</sub>)<sub>2</sub>, 0.82 MgSO<sub>4</sub>, 5 Tris (pH 7.4) supplemented with 50 µg/ml gentamycin and used for two-electrode voltage clamp electrophysiology (TEVC) measurements 2 to 7 days after injection.

*Intracellular Ca<sup>2+</sup> imaging assay* – For determination of concentration-response curves for glutamate activation and NAM inhibition of WT and mutant GluA2 receptors, imaging of changes in the concentration of intracellular Ca<sup>2+</sup> in transfected HEK293T cells were performed using a FlexStation I plate reader (Molecular Devices) to measure changes in the fluorescence of a calcium-sensitive fluorescent dye in 96-well plates. On the day of experiments, transfected cells were washed three times in PBSCM (in mM: 137 NaCl, 2.7 KCl, 10 Na<sub>2</sub>HPO<sub>4</sub>, 2 KH<sub>2</sub>PO<sub>4</sub>, 0.1 CaCl<sub>2</sub>, 0.5 MgCl<sub>2</sub>, pH 7.4) and loaded with a solution containing 2 µM Fluo-2 or Fluo-8AM fluorescent indicator dye (dissolved in plain DMEM and incubated for 30 min at 37 °C. Excess loading dye was removed by washing three times in FLUO buffer containing (in mM) 140 choline chloride, 5 KCl, 1 MgCl<sub>2</sub>, 10 CaCl<sub>2</sub>, 10 HEPES (pH 7.4). For NAM IC<sub>50</sub> experiments, cells were pre-incubated with 50 µl FLUO buffer containing various concentrations of NAM for 10 min at room temperature to achieve equilibrium before measurement of agonist responses. Maximum final NAM concentrations were 100 µM PMP, 100 µM CP, and 2 mM GYKI-53,655. The highest final dimethyl sulfoxide (DMSO) concentration was 4 % (v/v) for GYKI-53,655 and 0.2 % (v/v) for perampanel and CP-465,022. DMSO concentrations up to 4 % v/v had minimal effect on the glutamate responses in HEK293T cells (*data not shown*). Changes in dye fluorescence in response to the addition of agonist solution were then measured at 538 nm using excitation at 485 nm and emission cut-off at 515 nm. Baseline fluorescence was measured for 18 s before the addition of 50 µl agonist solution to each well

**MOL # 116871**

of the assay plate, and fluorescence was measured for 72 s after addition of the agonists. Peak fluorescence was calculated as the difference between maximal observed increase in fluorescence and pre-agonist baseline fluorescence. Agonist solutions were prepared in FLUO buffer in clear V-bottom 96-well plates (Thermo Fischer Scientific, Waltham, MA, USA) and contained 50  $\mu$ M CTZ and 300  $\mu$ M glutamate unless otherwise stated. Generally, experiments were performed in quadruplicate wells for each mutant and compound concentration and repeated on three independent days. Pre-incubation with NAMs in some instances produced a concentration-dependent inhibition of the baseline measurement before Glu addition, which resulted in an apparent increase in response amplitude with increasing NAM concentration. This effect likely arises from activation by small amounts of contaminating Glu produced by the cells which were not removed by thorough washing. The observation might indicate an effect of the desensitization state of the receptor on NAM potency.

*Determination of cell-surface expression* – For determination of mutational effects on cell surface expression of GluA2 receptors, mutants were created in a GluA2 subunit construct tagged with a bacterial  $\beta$ -lactamase enzyme (*blac*). Relative levels of surface-expressed *blac*-tagged GluA2 (*blac*-GluA2) can be accurately quantified in living cells by measuring the conversion rate of the membrane-impermeable substrate nitrocefin by simple absorption spectroscopy (Lam et al., 2013). For analysis in HEK293T cells, transfected cells were cultured in poly-D-lysine coated clear-bottom 96-well plates for two days. Cells were washed twice in PBSCM followed by addition of nitrocefin to a final concentration of 50  $\mu$ M in a total volume of 100  $\mu$ L per well. Immediately following nitrocefin addition, plates were placed in a microplate reader (Safire2, Tecan, Maennedorf, Switzerland) and well absorbance at 486 nm of the nitrocefin conversion product was recorded every minute for 60 minutes at  $\sim$ 30  $^{\circ}$ C. For each well, the absorbance at 486 nm (Abs486 nm) was plotted as a function of time using GraphPad Prism v6.01 (GraphPad Software, San Diego, CA, USA) and the rate of nitrocefin conversion per minute was determined by linear regression analysis of the slope of the curve in the linear range.

*TEVC electrophysiology* – For TEVC recordings, glass micropipettes (0.69 mm ID/1.2 mm OD, Harvard apparatus, Holliston, MA, USA) were pulled on a Sutter P-1000 to a tip resistance of 0.5-2.5 M $\Omega$  and filled with 3 M KCl. Oocytes were clamped using a two-electrode voltage-clamp amplifier (OC-725C, Warner Instruments, Hamden, CT, USA) and continuously perfused with Frog Ringer's solution containing (in mM) 115 NaCl, 2 KCl, 5 HEPES, and 1.8 BaCl<sub>2</sub> (pH 7.6 with NaOH) via the force of gravity at flow rates of 5 to 10 mL/min into a vertical oocyte flow chamber with a volume of 0.3 mL (Joshi et al, 2004). Compounds dissolved in Frog Ringer's solution were added by bath application. This perfusion system yields a solution exchange time of 100 to 500 ms. Concentration-response data were generally recorded at a holding potential of -30 or -60 mV, and each compound solution was applied for 30 or 45 s to ensure that steady-state currents were obtained. NAM concentration-response curves were obtained by adding increasing concentrations of NAM in the continuous

**MOL # 116871**

presence of 300  $\mu\text{M}$  glutamate after evoking a full agonist response by adding 300  $\mu\text{M}$  glutamate alone. All experiments were performed at room temperature (20 to 23  $^{\circ}\text{C}$ ). Data acquisition was accomplished using a CED 1401plus analog-digital converter (Cambridge Electronic Design, Cambridge, UK) interfaced with a PC running WinWCP software (available from Strathclyde Electrophysiology Software, University of Strathclyde, Glasgow, UK). Concentration-response and concentration-inhibition measurements were performed by measuring agonist-evoked current during step-wise application of increasing concentrations of agonist or NAM as illustrated in Figure 6.

*Patch-clamp electrophysiology (HEK cells)* – For electrophysiological experiments involving rapid ligand-application measurements, outside-out membrane patches were excised from transiently-transfected HEK293 cells using thin wall glass micropipettes (TW150F-4, World Precision Instruments) heat polished to 3-10  $\text{M}\Omega$  tip resistance filled with internal solution containing (in mM) 140 KCl, 10 HEPES, 1 BAPTA, pH 7.20 with KOH, osmolality adjusted to 285 mOsm by adding 10 mM D-Glucose. Pipettes had a tip resistance of 3-10 $\text{M}\Omega$ . External recording solution for all experiments were comprised of (in mM) 150 NaCl, 3 KCl, 10 HEPES, 0.01 EDTA, 1  $\text{CaCl}_2$ , pH 7.40 with NaOH, 290 mOsm. Currents were recorded at a holding potential of -60 mV with an Axopatch 200B amplifier (Molecular Devices), low-pass filtered at 8 kHz using an 8-pole Bessel filter (Frequency Devices, Ottawa, IL, USA), and digitized at 40 kHz using a Digidata 1440A (Molecular Devices). Rapid application and removal of ligand solutions at excised membrane patches were performed using a piezo (Burleigh Instruments, Fishers, NY) bimorph-driven double-barreled theta tube perfusion system. The time course of solution exchange across the laminar flow interface was estimated by liquid junction potential measurements of 0.2-0.4 ms (10-90% rise time) for a 10-fold difference in ionic strength. Current kinetics was analyzed using ChanneLab v2 (Synaptosoft, Decatur, GA, USA).

*Data and statistical analysis* – For construction of concentration-response curves from  $[\text{Ca}^{2+}]_i$  imaging experiments, peak fluorescence response (corresponding to the difference between the maximum and baseline 538 nm emission) from quadruplicate wells representing identical NAM or agonist concentration were averaged using SoftMax Pro v5.4 software (Molecular Devices, Sunnyvale, CA, USA). For each individual plate experiment, the average responses were normalized to the average corresponding maximal agonist response or the agonist response in absence of NAM. Composite concentration-response curves were generated by plotting normalized data from multiple experiments as a function of NAM or agonist concentration using GraphPad Prism software. Concentration-response relationships were fitted as composite curves using GraphPad Prism v6.01 (GraphPad Software, San Diego, CA, USA) to the Hill equation:

$$\text{response} = \text{bottom} + \frac{\text{top} - \text{bottom}}{1 + 10^{(\log X C_{50} - X) \cdot nH}}$$

where *bottom* is the fitted minimum response, *top* is the fitted maximum response, *nH* is the Hill slope, and *X* is the concentration, and  $X C_{50}$  is the  $IC_{50}$  (half-maximally effective concentration of inhibitor) or  $EC_{50}$  (half-

**MOL # 116871**

maximally effective concentration of agonist), respectively. For the construction of concentration-response curves from electrophysiological data, agonist-evoked current responses from individual oocytes were determined from TEVC traces using ClampFit v10.3 (Molecular Devices) and normalized to the current response obtained in the absence of NAM (for  $IC_{50}$  determinations) or by maximal agonist concentration (for  $EC_{50}$  determinations). Concentration-response curves were constructed as composites of normalized responses from 3 to 6 oocytes and analyzed as described for the  $[Ca^{2+}]_i$  assay. Unless otherwise noted, results are expressed as mean  $\pm$  SD. Statistical analysis of pairwise and multiple comparisons was performed using Student's t-test or ANOVA with multiple comparison procedures as indicated.

*Molecular modeling* – The crystallographic structures of the GluA2 receptor used as input models for ligand docking included the *apo* state structure (PDB 5L1B), the GYKI-bound structure (PDB 5L1H), the CP-bound structure (PDB 5L1E) and the PMP-bound structure (PDB 5L1F). All structures were determined by Yelshanskaya *et al.* (2016) and obtained from the Brookhaven Protein Data Bank (Berman *et al.*, 2000). All four structures have several missing residues and residues with missing side chain atoms. For the initial docking calculations, missing atoms in locations that are distant from the NAM binding sites, located at the extracellular side of the transmembrane domain, were not modeled; this includes residues located in the ATD-LBD linker region, the M1-M2 linker region, and the C-terminal region. Within and around the NAM binding pockets, positions with missing atoms are located in the S1-M1 linker region, the M3 transmembrane helix, the M3-S2 linker, and the S2-M4 linker. For these regions the missing atoms were added using the WHAT-IF webserver interface (Vriend, 1990) following the method described by Chinae *et al.* (Chinae *et al.*, 1995). The ligand molecules co-crystallized with the GluA2 receptor in PDB files 5L1H, 5L1E and 5L1F were imported into the Maestro software (Schrödinger Release 2013-2: Maestro, Version 9.5, Schrödinger, LLC, New York, 2013), where hydrogen atoms were added. The ligands were either left in the crystal conformation or subjected to a short energy minimization using the “clean up geometry” function; giving rise to two conformations for each imported structure. The original ligand structures (with hydrogen atoms added) and the equivalent energy-minimized structures were used as input for docking calculations, i.e. in total eight structures per ligand from the four different subunits, each in either original or optimized conformation. Additionally, for each ligand two conformations were generated by constructing the ligand from scratch in Maestro, meaning that 10 input ligand structures were used for docking of each of the ligands CP, PMP, and GYKI. PMP, CP, and GYKI have low solubility in water, suggesting that they are neutral at physiological pH, and were therefore docked in their unprotonated states. All ligand docking into the GluA2 receptor structures was performed using the Autodock Vina docking software (Trott and Olson, 2010), utilizing a search box that covered all four binding pockets. 20 poses were saved in each docking run during which the ligands were treated flexibly, while the protein remained rigid. In general, the poses showed variation in the position of the ligand due to the relatively large search box.

**MOL # 116871**

However, the binding pocket was identified for all three ligands when docked into their “parent” protein structure and assumed orientations similar to those proposed by the existing GluA2/NAM structures (Yelshanskaya et al., 2016). Based on the assumption that these ligand orientations are overall correct, we constructed up to 100 models for each compound (98 for GluA2:GYKI, 99 for GluA2:PMP and GluA2:CP), i.e. generating approximately 400 binding sites as the NAM:GluA2 stoichiometry, at least in the crystal structures, is 4:1. In this alternative approach, different side chain conformations were sampled around the ligand-binding sites using modeling software MODELLER (Sali and Blundell, 1993) to build models of the GluA2/NAM complex for which all missing atoms and residues were added. Furthermore, all residue positions within 12 Å of the ligands were optimized. MODELLER can accommodate the ligands in terms of space, but without parameters for the ligands the interactions with the protein atoms of the binding site are not included in the optimization. Thus, to account for protein-ligand interactions and to optimize the ligand conformations, all the generated models were subjected to an energy minimization in GROMACS 5.0 (Van der Spoel et al., 2005) using the AMBER99-ILDN (Lindorff-Larsen et al., 2010) force field for the protein and ligand parameters from the general AMBER force field (GAFF) (Wang et al., 2004) generated using Antechamber in AmberTools14 (Salomon-Ferrer et al., 2013). Acypype (Sousa da Silva and Vranken, 2012) was used to generate Gromacs topologies from the Amber ones. Minimizations were performed in vacuum until the maximum force on a single atom was less than 100 kJ/mol/nm or machine precision was reached. Analysis and image generation were performed using the Maestro software along with VMD (Humphrey et al., 1996) and PyMOL software.

## 7. Results

*Glycine-scanning mutagenesis of the S1-M1 and S2-M4 linker regions* – Previous mutational analysis had identified the LBD-TMD linker segments as overall candidate regions to form the NAM binding sites in the AMPAR complex (Balannik et al., 2005). Specifically, mutation of residues in the S1-M1 and S2-M4 segments can perturb NAM inhibition and these residues may thus be involved in forming NAM binding pocket as well as interact directly with NAMs (Fig. 1). However, the NAM binding site likely involves additional residues in the linker segments as well as upper M1 and M4 segments. To expand the knowledge of the contribution of the side chains of individual residues in the S1-M1 (including the preM1 helix), upper M1, S2-M4 and upper M4 segments for NAM binding, we initially performed Gly scanning mutagenesis of all amino acid positions between K511 and M527 in the S1-M1 and upper M1 segment and between E782 and Y797 in the S2-M4 and upper M4 segment (Fig. 3). We selected the *flip* isoform of the GluA2 subunit in the unedited form as the model AMPAR subunit for the mutational study based on the robust expression and well-characterized functional properties of homomeric GluA2 receptors. In addition, several X-ray crystallographic and cryo-EM structures exist for homomeric GluA2 receptors (Sobolevsky et al., 2009; Twomey et al., 2016; Twomey et al., 2017b; Yelshanskaya et al., 2014), which provide an excellent framework for interpreting mutagenesis results in a structural context and can serve as target structures for ligand-docking. Notably, the target LBD-TMD linker regions are conserved between subunits GluA1-4. Thus, if the NAM binding sites are harbored in the linker region, homo- or heteromeric AMPARs formed of any subunit combination may potentially be equivalent with regards to the structure of the NAM binding pocket. To allow determination of mutational effects on surface expression, we used a version of GluA2 tagged in the *N*-terminal of the ATD with the reporter enzyme *blac* (*blac*-GluA2; *Materials and Methods*) as parent construct for all mutants. To ensure that fusion of *blac* to the ATD does not change the function of the GluA2 receptor, we compared current responses from WT GluA2 and *blac*-GluA2 in excised outside-out membrane patches from HEK293 cells to the application of a maximally effective concentration (10 mM) of glutamate; using a rapid perfusion system with a solution exchange time < 0.4 ms (*Materials and methods*) (Supplemental Fig. S1). The results showed that the rates of receptor activation, desensitization, and deactivation were similar with and without *blac* fused to the ATD (Supplemental Fig. S1). Furthermore, we determined the  $IC_{50}$  for NAM inhibition of WT GluA2 and *blac*-GluA2 currents in *Xenopus* oocytes (*Materials and methods*) and did not observe any significant effect of *blac* on NAM pharmacology (Supplemental Fig. S1 and Table 1 and 2).

For initial characterization of the mutant library, we expressed mutants individually in HEK293 cells and used an intracellular calcium concentration ( $[Ca^{2+}]_i$ ) imaging assay to measure concentration-dependent Glu-evoked increases in  $[Ca^{2+}]_i$  (*Materials & Methods*) and assessed the impact of Gly substitutions on basal receptor function by determining the  $EC_{50}$  and maximum response amplitude ( $E_{max}$ ) for Glu (Fig. 2). Also, we measured

**MOL # 116871**

*blac* activity to determine mutational effects of the ability of the mutant GluA2 subunits to correctly fold, assemble, and traffic to the cell surface (Supplemental Fig. S2 and Supplemental Table 1). The results of the Gly scanning mutagenesis are summarized in Fig. 3 and Table 1. For the 16 positions in the S1-M1 and upper M1 segments, Gly substitution (which removes the WT residue side-chain) appeared to disrupt receptor function at five positions (L518, P520, L521, I525, and W526) as these mutants, when expressed in HEK293 cells, did not produce clearly detectable  $\text{Ca}^{2+}$  signals in the  $[\text{Ca}^{2+}]_i$  imaging assay in response to Glu concentrations up to 1 mM (see Fig. 2A for a representative example). However, expression of all five mutants generated extracellular *blac* activity in HEK293 cells that were within the range of the activity observed for expression of WT *blac*-GluA2 receptors (Supplemental Table 1); indicating that these Gly substitutions maintain the ability of the GluA2 subunit to fold and traffic to the cell surface. These results suggest that Gly substitutions at these positions may alter or completely disrupt receptor function. The Gly mutants for the remaining 11 positions displayed robust Glu-evoked  $\text{Ca}^{2+}$  signals that allowed determination of Glu  $\text{EC}_{50}$  values. For the majority of functional mutants, Glu  $\text{EC}_{50}$  was identical to or within three-fold range of the  $\text{EC}_{50}$  value for WT *blac*-GluA2 (Table 1 and Fig. 3). For the 15 Gly substitutions in the S2-M4 and upper M4 segments, four mutants (L787G, V792G, F796G, Y797G) were non-functional with intact cell surface expression (Supplemental Fig. S2 and Supplemental Table 1), whereas Gly substitution at the remaining 11 positions yielded mutants with robust Glu-evoked responses and  $\text{EC}_{50}$  values that were unchanged or within three-fold range of WT *blac*-GluA2 (Fig. 3B). Thus, in total we generated 31 Gly mutants of which 22 were functional and could be subjected to characterization of potential changes in GluA2 NAM pharmacology.

*Effect of glycine substitutions on inhibitory potency of perampanel, CP and GYKI* – We next used the  $[\text{Ca}^{2+}]_i$  imaging assay to generate full concentration-inhibition relationships for PMP, CP and GYKI (*Materials and methods*) to determine the  $\text{IC}_{50}$  for each NAM across all functional Gly mutants (Table 2). Representative examples of concentration-response curves are shown in figure 4, and figure 5 summarizes the relative changes in NAM potency produced by the Gly substitutions compared to WT *blac*-GluA2. Determination of specific  $\text{IC}_{50}$  values was not possible at some mutants that displayed decreased sensitivity to NAMs due to limitations in NAM solubility.

For the S1-M1 segment, we generally observed similar patterns of mutational effects for the three NAMs (Fig. 5). Specifically, removal of residue side chains at K511 and V514 produce loss-of-potency for PMP, CP, and GYKI, whereas removal at F517 produces gain-of-potency effects for all three NAMs (albeit only three-fold for CP at F517G) (Fig. 5 and Table 2). The similar effect patterns suggest that the S1-M1 linker is involved in NAM binding or inhibitory mechanism, and furthermore corroborates the previous suggestions that PMP, CP, and GYKI have overlapping binding sites (Hanada et al., 2011; Menniti et al., 2000). For GYKI, additional changes in potency occur by removal of the F515 and D519 side chains (leading to gain-of-potency), and the

**MOL # 116871**

S516 side chain (leading to loss-of-potency). These results indicate that GYKI might interact with additional residues in the S1-M1 region compared to PMP and CP. For the Gly mutations in the upper M1 segment (A522G to M527G), no substantial potency changes (here defined as more than a five-fold change in  $IC_{50}$ ) were observed for any NAM (Fig. 5 and Table 2); indicating that the upper M1 transmembrane domain may not be involved in NAM binding. However, notably only four Gly mutants within the M1 region were characterized as the I525G and W526G mutants were not functional in the  $[Ca^{2+}]_i$  assay and thus not amenable to pharmacological characterization.

For Gly mutants of the seven positions in the S2-M4 segment, A786G displayed a gain-of-potency effect for PMP and GYKI, whereas the remaining Gly substitutions did not change the potency of any of the NAMs substantially (Fig. 5). In the upper M4 segment, no substantial changes in NAM potencies were seen upon Gly substitutions from L789 to V795 (Fig. 5). The exception to this pattern is the effect of the N791G mutation for CP potency, for which removal of the asparagine side chain decreases the  $IC_{50}$  of CP by more than ten-fold, whereas PMP and GYKI potency does not substantially change.

In summary, we assessed the effects of Gly substitutions on NAM potency for 11 positions in the S1-M1/upper M1 segments and 11 positions in the S2-M4/upper M4 segments. Among these positions, six Gly substitutions in the S1-M1 segment displayed more than a five-fold change in  $IC_{50}$ , whereas no effects were observed for the upper segment of the M1 transmembrane helix. Furthermore, one substitution in the S2-M4 region and one substitution in the upper M4 segment displayed substantial effects. These results of the Gly scan thus overall implicate eight residues in potential formation of the NAM binding site in GluA2.

*Mutational analysis of key NAM binding pocket residues* – To assess the role of side chains at the initial positions identified in the Gly scan (Fig. 5), we made additional mutants of potential key positions to introduce side chains with different physicochemical properties (e.g. change the bulk size and/or change of hydrogen bonding properties of the side chain). Positions included mainly those where Gly substitution induced more than five-fold change in NAM potencies or was previously reported to change NAM activity (Balannik et al., 2005) (Fig. 5). At this point of the mutational analysis, X-ray crystallography structures were reported of homomeric GluA2 in complex with the same NAMs included in the present study (PMP, GYKI and CP) (Yelshanskaya et al., 2016); showing that four nearly identical NAM binding sites are located within the LBD-TMD linker region of the tetramer. Although the electron densities around the identified NAM binding pockets in all the GluA2/NAM structures were insufficient to resolve several protein residue side chains, the structures provide unambiguous identification of the segments that form the binding pocket. Specifically, each NAM binding pocket is formed almost exclusively within each subunit by segments in the subunit S1-M1 linker (from K509 to P520, including the preM1 helix) and the extracellular facing regions of the M4 helix (from L787 to V795) and the M3 helix (from Y616 to R628). The identification of these parts of the S1-M1 and upper M4 segments were

**MOL # 116871**

in good agreement with the results from the Gly scan in that all of the eight positions identified to change NAM potency upon Gly substitution are contained herein (Fig. 5). Also, the GluA2/NAM structures suggest that several residues within the upper M3 segment are in proximity to form direct interactions with the NAMs (Y616, L620, and F623, and S615 from the neighboring subunit). We included mutations of three of these residues to probe their potential involvement for direct interactions with the NAMs.

In total, we made additional mutations at 16 positions (Fig. 7) and determined effects on NAM potency using the  $[Ca^{2+}]_i$  assay (Table 2). Also, we subjected selected mutants to determination of NAM potency using TEVC electrophysiology that more directly measures AMPAR activation. Specifically, we expressed mutant and WT GluA2 receptors in *Xenopus* oocytes and determined NAM  $IC_{50}$  for inhibition of steady-state agonist-evoked currents (*Materials and methods*). The standard recording protocols are illustrated in Fig. 6. In general,  $IC_{50}$  values obtained from the TEVC experiments were lower than those obtained from the  $[Ca^{2+}]_i$  experiments (Table 2). For example, PMP and GYKI display  $IC_{50}$  values for WT GluA2 that are five- and ten-fold lower than the corresponding values obtained in  $[Ca^{2+}]_i$  experiments (Table 2). Additionally, relative changes in NAM potencies for mutants investigated by TEVC electrophysiology were generally smaller than the changes observed in the  $[Ca^{2+}]_i$  assay. It should be noted that during agonist-application in the  $[Ca^{2+}]_i$  assay, desensitization is inhibited by co-application of cyclothiazide (CTZ) in order to produce robust  $Ca^{2+}$  responses (see *Materials and Methods*), whereas desensitization is not blocked during TEVC recordings. The difference in CTZ co-application with NAM may underlie these differences as previous work has shown that CTZ, which binds in the LBD dimer interfaces to stabilize in a non-desensitizing conformation (Sun et al., 2002), allosterically influences the distinct NAM binding site to decrease apparent inhibitory potency (Johansen et al., 1995).

We created additional mutants at eight positions within the pre-M1 helix, the flanking S1-M1 linker segments, and the upper M1 and determined NAM potency (Fig. 7). At three positions in the preM1 helix (V514, F515, and F517), Gly substitutions indicated potential roles for NAM potency (Fig. 5). As Gly has no side chain, Gly mutation is excellent for disrupting all potential ligand-protein interactions with the residue side chain. However, Gly also introduces flexibility to the protein backbone that might perturb local secondary structure or exert allosteric effects on the adjacent binding pocket structure. We, therefore, mutated V514, F515, and F517 to Ala to reduce their hydrophobic side chains, but maintain backbone structural constraints. Also, for the L518 position, where Gly substitution destroyed measurable activity, we created the functional L518A mutant to probe the effect of shortening the hydrophobic side chain. In general, we considered performing Ala substitutions at all positions where Gly substitution produced non-functional receptors; in particular for residues with large hydrophobic side chains (such as for example W526 in M1 and F796 and Y797 in M4 region) in order to create potentially functional mutants that would enable characterization of the impact of side chain reduction on NAM

**MOL # 116871**

potency. However, as GluA2/NAM structures were available at this point in the mutational analysis, we excluded residues that appeared to be outside the NAM binding pockets from further analysis under the assumption that further substitutions of such residues was outside the primary aim of this part of the mutational analysis, which focused on probing potential direct ligand contacts. In agreement with previous observations (Yelshanskaya et al., 2016), Ala substitutions at F515, F517, and L518 generally produced no or minor changes in NAM potency. For F515 and F517, these results indicate that the observed changes by Gly substitutions may involve allosteric effects. In contrast, the V514A mutation produced reductions in potency for all NAMs that were similar to those produced by the V514G mutation (Fig. 7). To further explore V514, we mutated this residue to Asp (introducing a negatively charged side chain) and Trp (increasing side chain size). Interestingly, the pattern of effects of these mutations differed among the NAMs, with GYKI potency being reduced at V514D and V514W, whereas PMP and CP were not affected or displayed smaller increases in  $IC_{50}$  of up to five-fold (Fig. 7). In the GluA2/NAM structures, V514 appears to be located outside the binding pocket (Fig. 7). Thus, the effect pattern of large decreases by Gly and Ala substitutions and less effect of Asp and Trp substitutions may not result from perturbation of direct interactions between the NAMs and the V514 side chain, but rather reflect a role of V514 in shaping the NAM binding site.

At position D519 in preM1 and A522, Y523, and E524 in upper M1 (Fig. 7), we made further mutations based on previous reports of combinations of mutations at these positions in GluA3 and GluK2 to change NAM potency (Balannik et al., 2005). D519N displayed decreased potency for CP, which is in agreement with a suggested role of the  $\gamma$ -carboxylate in direct interaction with CP (Yelshanskaya et al., 2016). No other single mutations at A522, Y523, and E524 produced substantial effects on NAM potency (Table 2 and Fig. 7). These results are in contrast to the previously suggested roles of these residues in interaction with GYKI (Balannik et al., 2005), but in general agreement with their positions outside the NAM binding pockets in the GluA2/NAM structures (Fig. 7).

We created additional mutants at five positions within the S2-M4 linker and upper M4 region (Fig. 7). The mutations were observed to produce similar effect patterns on PMP and GYKI potency in the  $[Ca^{2+}]_i$  assay (Table 2 and Fig. 7), which both were sensitive to mutations at N791 and insensitive to mutations at V792, A793, and G794 (Fig. 7). In contrast, CP displayed sensitivity towards mutation at all positions (Table 2 and Fig. 7), despite side chains of position 792 to 794 being located outside the NAM binding pocket. In the TEVC experiments, the effects on NAM potencies by mutations at V792, A793 and G794 were generally less than three-fold, indicating that neither of these residues forms key interactions with the NAMs (Table 2).

In the M3 segment, we created three mutants (Fig. 7). The mutant Y616F probes the potential hydrogen bonding properties of the side chain hydroxyl for NAM binding. Y616F did not display sufficient activity in the  $[Ca^{2+}]_i$  assay, but we were able to characterize the mutant using TEVC electrophysiology and found no

**MOL # 116871**

substantial effect on NAM potency, suggesting that the side chain hydroxyl is not involved in direct ligand interactions. The mutant S615A also removes a side chain hydroxyl and displayed substantial loss-of-potency for PMP and GYKI in the  $[Ca^{2+}]_i$  assay (Table 2 and Fig. 7) in agreement with the previously reported effect of this mutation (Yelshanskaya et al., 2016). However, the S615A mutation did not change PMP and GYKI potencies measured by TEVC electrophysiology. Moreover, the mutant displayed a gain-of-potency effect for CP in TEVC, but not in the  $[Ca^{2+}]_i$  assay (Table 2). These results may indicate that the role of the S615 residue in NAM function differs depending on the desensitization state of the receptor, as desensitization is blocked by addition of CTZ in the  $[Ca^{2+}]_i$  assay and the patch-clamp experiments performed by (Yelshanskaya et al., 2016), but not in our TEVC experiments. In order to investigate the effect by addition of CTZ at the S615A mutant, we conducted TEVC recordings to determine NAM potencies at WT and S615A mutant receptors in the presence of CTZ (Supplemental Fig. S3 and Supplemental Table 2). The presence of CTZ only caused minor (less than three-fold) effects on NAM  $IC_{50}$  at WT GluA2 and *blac*-GluA2 receptors. However, in the presence of CTZ, the S615A mutant displayed substantial loss-of-potency for PMP and GYKI and no change in CP potency, similar to the results obtained in the  $[Ca^{2+}]_i$  assay, and the previously reported effect of the S615A mutation on PMP and GYKI potency (Yelshanskaya et al., 2016). These results indicate that blocking desensitization affects the role of S615 in NAM inhibition. F623A displayed substantial loss-of-potency for PMP and CP in both the  $[Ca^{2+}]_i$  and TEVC assays; supporting a role of the side chain phenyl group in direct ligand interactions as previously suggested (Yelshanskaya et al., 2016).

*Generation of NAM binding models in GluA2* – The GluA2/NAM crystal structures have inadequate resolution in the NAM binding pockets for assignment of side chain conformations for many residues around the bound NAMs and therefore provide limited information on specific ligand-protein interactions. To address this issue, Yelshanskaya *et al.* modeled several side chains based on conformations observed in a higher resolution structure of GluA2 obtained in complex with the competitive antagonist ZK200775 (PDB code 3KG2)(Sobolevsky et al., 2009) and then used docking calculations to create models of NAM binding modes. However, the GluA2/ZK200775 structure also has several side chains missing in the NAM binding pocket, and these were therefore not modeled in the docking calculations (M. Kurnikova, personal communication). The missing side chains close to the NAM binding pocket include K508, K509, K511, E627, R628, E782, K783, and T784. Thus, the conformations of several side chains that might form critical interactions with PMP, CP and GYKI remain unknown. We, therefore, repeated the docking with the inclusion of the missing side chain atoms in the binding sites using the GluA2/NAMs structures as template (*Materials and Methods*). Initially, we employed a docking procedure with flexible ligand docked into a rigid NAM binding pocket. To make the search as unbiased as possible, the search box used for the docking calculations was made large enough to include all four binding sites as well as the majority of the TMD and the nearest part of the LBD. Of the 200 generated

**MOL # 116871**

poses for each ligand (10 input conformations x 20 poses per docking), at least 25% show the ligand positioned in the binding site (27% for PMP, 35% for GYKI and 79% for PMP). The remaining poses are located either in the pore, between transmembrane helices or in between TMD and the LBDs. The ligand poses in the binding sites show considerable variability, possibly because only very few HBs are formed. However, we confirmed that poses similar to the binding modes observed in the crystal structures by Yelshanskaya *et al.* (2016) could be identified for each of the three ligands. The predicted binding energies for poses docked in the binding sites for all three ligands are similar, ranging from -7.4 kcal/mol to -10.5 kcal/mol; comparable to the results presented previously (Yelshanskaya *et al.* 2016). Thus, when docked into the GluA2/NAM structures with all side chains around the binding site added, all three NAM ligands can find binding modes very similar to those suggested by Yelshanskaya *et al.* (Yelshanskaya *et al.*, 2016) (Supplemental Fig. S4). On this basis, we proceeded with the ligand orientations that were proposed from the GluA2/NAM structures to create three sets of binding models based on sampling flexible side chain orientations followed by energy minimizations to generate a total of 400 binding site models for each ligand (*Materials and methods*). Each model set represents a range of possible conformations of all binding pocket side chains and their potential ligand/protein interactions. Figure 8 illustrates the observed variability in side chain orientation for all residues within 5 Å of the NAMs (26 residues in total). For all three NAMs, we find the majority of proposed protein/ligand interactions to be primarily hydrophobic. Specifically, among the 26 residues surrounding the NAMs, 14 are purely hydrophobic, and four are mostly hydrophobic with a single polar group (K509, K511, Y616, and W526). Notably, the positions of the hydrophobic side chains show only very little variability among models. In contrast, the side chain of K511, which is not resolved in the GluA2/NAM X-ray crystal structures (Yelshanskaya *et al.*, 2016), displays a wide range of conformations with the K511 side chain pointing towards the NAM molecules in some models, and more towards the lipid bilayer region in others. Figure 9 shows a representative model for each NAM, representing frequently observed side chain orientations among the 400 models. For PMP, the phenyl ring of PMP is frequently stacked between F623 and P520 (Fig. 8A and 9A); similar to the proposal by (Yelshanskaya *et al.*, 2016). F517 and V795 are lining the tip of the PMP pyridine ring, and the benzo-nitrile is lined by P512 and the carbon chain of K511. Similar to the X-ray crystal structures (Yelshanskaya *et al.*, 2016), the methylene-dioxy group of GYKI is stacked against F623 (Fig. 8C and 9C). The amino-phenyl group of GYKI is surrounded by a hydrophobic pocket consisting of F517, P520, L620, L624, and L787, and the 5-methyl group is lined by P512 and the carbon chain of K511. The quinazolinone moiety of CP surrounded by F517, P520, I611, L620, L787, V792, and V795, and the pyridine moiety is orientated parallel to F623 with its amino-substituent lined by the carbon chain of K511 and the cyano-phenyl points toward L787 and L624 (Fig. 8B and 9B).

In terms of potential hydrogen bond (HB) interactions, the NAM molecules may form HBs to both side chain or backbone atoms of the protein. Ten residues are overall observed within 5 Å distances of the NAM

**MOL # 116871**

ligands that have side chains containing HB donor or acceptor moieties (Fig. 8 and 9). Bulk analysis of the orientations of these side chains in the model sets showed five of these (S510 and K511 in the S1-M1 linker, S516 in the preM1 helix, S615 and Y616 in the upper M3 helix, and N791 in the upper M4 helix) to frequently be oriented to potentially form HB interactions to one or more of the NAM ligands with reasonable bond angles. It should be noted that the initial side chain orientations for the optimized models are generated using MODELLER (Sali and Blundell, 1993), which ensures that there is space for the ligands but does not take the chemical nature of the ligand into account. The models are subsequently energy minimized to optimize the protein-ligand interactions, using proper parameters for the ligands. However, the minimization will only locate a nearby local minimum, so if a side chain is not reasonably close to the ligand initially, it will not form a HB during a minimization. Thus, the method may not allow for the identification of all possible HBs, and the frequency of a given HB is not necessarily a measure of the importance of that HB for the binding of the ligand. However, the method allowed us to identify several possible HBs that were not indicated in the crystal structures or through docking. With this in mind, the five residues (K511, S516, S615, Y616, and N791) can be considered as potential key HB interaction points for NAM binding (Supplemental Fig. S5-S7). Of these, K511 has not previously been suggested as an interaction point as the side chain was not resolved or modeled in the GluA2/NAM X-ray crystal structures (Yelshanskaya et al., 2016). For PMP and GYKI, three side chains are implicated in potential HB interaction with the ligand (K511, S516, and N791 for PMP and S510, S615, Y616 and N791 for GYKI), whereas only N791 is suggested for CP (Fig. 9). The side chain of N791 is thus suggested to participate in HB interactions with all three NAMs, similar to the proposal by (Yelshanskaya et al., 2016).

For PMP, the side chain most frequently observed in an orientation to form potential HBs was N791, through the interaction of the  $\delta$ -amide group of N791 with either the pyridine nitrogen or the nitrile of PMP (45% of our models in total; Supplemental Fig. S5). The  $\gamma$ -hydroxyl group of the S516 side chain was within distance for HB formation with the nitrile of PMP as suggested by (Yelshanskaya et al., 2016) in 28% of the models. The  $\zeta$ -ammonium group of the K511 side chain was less frequently (14% of the models) within distance for interaction with the nitrile and/or the carbonyl groups of PMP. Potential HB interactions between PMP and the side chains of S615 or Y616 as suggested by (Yelshanskaya et al., 2016) were generally not observed in our models. For GYKI, N791 was also frequently observed in an orientation to form potential HB interactions, through interaction of the  $\delta$ -amide group of N791 with the amide oxygen and/or the benzodiazepine nitrogen of GYKI (26% and 33% of the models, respectively; Supplemental Fig. S7). Similar to the X-ray crystal structures (Yelshanskaya et al., 2016), the  $\gamma$ - and  $\eta$ -hydroxyl groups of S615 and Y616 were within distance for hydrogen bonding with the amine of GYKI in 72% and 75% of the models, respectively. In contrast with suggestions by Yelshanskaya *et al.* (2016), the  $\gamma$ -hydroxyl group of the S516 and S788 side chains were infrequently or not at all within distance to form HB interactions with GYKI in our models. For CP, the  $\delta$ -amide group of N791 was

**MOL # 116871**

within distance of the carbonyl of CP in 52% of the models (Supplemental Fig. S6). Backbone-mediated HBs were not frequently observed in the models. Specifically, the analysis only suggests the backbone amide hydrogen of K511 to be oriented for potential HB interaction with the amide oxygen of GYKI (in 35% of the models) and with the nitrile of PMP (in 24% of the models) (Supplemental Fig. S5-S7). In general, in combination with the GluA2/NAM structures, our models fit well with most of the key experimental observations from the mutational analysis and provide an additional framework for understanding molecular details of AMPAR interactions with NAMs of three different chemical classes.

## 8. Discussion

The molecular pharmacology of AMPARs involves multiple binding pockets targeted by many chemical classes of exogenous ligands acting as synthetic agonists, channel blockers, competitive antagonists, PAMs, and NAMs. The location, structure and molecular properties of binding pockets for competitive antagonists (Sobolevsky et al., 2009), agonists (Durr et al., 2014; Twomey et al., 2017a; Yelshanskaya et al., 2014; Zhu and Gouaux, 2017) and positive modulators (Durr et al., 2014; Twomey et al., 2017a; Yelshanskaya et al., 2014; Zhu and Gouaux, 2017) are now defined at atomistic level in the context of near full-length tetrameric AMPAR structures; leading to detailed models for how these ligands influence AMPAR dynamics to modulate function. In contrast, progress in NAM molecular pharmacology has been limited, and essential aspects of NAM binding and functions have remained unknown. This is surprising since NAMs at present is the only class of AMPAR ligands from which a compound has emerged to become a therapeutic drug in humans. In the present study, our first aim was to use mutational analysis to pinpoint specific residues within the LBD-TMD linker regions as candidates for forming direct protein-ligand interactions. Our second aim was to use the mutational data to construct NAM binding models using existing GluA2 structures as docking templates. During work on both aims, X-ray crystallography structures of homomeric GluA2 in complex with the same prototypical NAMs selected for our study were reported (Yelshanskaya et al., 2016); thereby unambiguously identifying the number, location, and overall structure of the NAM binding pockets. However, the resolution of the X-ray structures was not sufficient for unambiguous identification of specific ligand-protein interactions involved in NAM binding. Thus, the data from our mutational analysis in combination with the recent GluA2/NAM structures form an improved basis for the construction of detailed binding mode models, which can be used for detailed analysis of ligand-protein interactions and serve as framework for beginning to understand all molecular aspects of NAM function at AMPARs.

Overall, our mutational data fitted well with the GluA2/NAM structures as most mutations changing NAM potencies were located in or near the NAM binding pockets, and these residues may thus potentially be critical for shaping the pocket or for direct ligand interactions. Some of these mutations concerned residues that were not resolved in the crystal structures. For example, we find that K511 in the S1-M1 linker is important for the potency of all three NAMs (Fig. 5 and Table 2). Mutational effects at K511 could not be interpreted from the existing GluA2/NAM structures as the side chain of K511 is not resolved or modeled (Yelshanskaya et al., 2016). Our results from the side chain optimizations suggest that K511 can adopt a position to form HBs with the NAM ligands, either by interaction with the side chain  $\zeta$ -ammonium group or with the backbone hydrogen (Fig. 8 and 9). Also, the aliphatic carbons of the K511 side chain may line up against hydrophobic moieties of the NAMs and may thus form hydrophobic interactions. Interestingly, in other GluA2 structures for which the side chain of K511 has been resolved, several different conformations and orientations of the K511 side chain

**MOL # 116871**

are observed. These include structures in which the side chain is orientated such that the primary amine points directly towards the empty NAM binding pocket (e.g., PDB codes 4U4F and 4U4G) (Yelshanskaya et al., 2014). In other structures, the K511 side chain points towards the membrane region; such as observed in a recently determined structure of a heteromeric GluA1/2 receptor in complex with the TARP  $\gamma 8$  (PDB code 6QKC)(Herguedas et al., 2019). Interestingly, in this structure, the K511 side chain is pointing directly towards the extracellular region of  $\gamma 8$  and a membrane lipid molecule. Hence, the variation in side chain conformations observed in the modeling appears convincing. Because we only tested mutation of K511 to Gly, and Gly introduces backbone flexibility, it is plausible that the mutation may have affected hydrogen bonding capacities of both the backbone and side chain as well as hydrophobic interactions of the aliphatic carbons. Thus, our models and mutational data together point towards K511 as a novel interaction point for the NAMs. However, there are also examples of mutations of residues that we find to exert substantial effects on NAM potencies that cannot be readily explained by direct interactions in the current structures or our models. For example, V514 in the S1-M1 linker region is in the periphery of the binding pocket, and its side chain is pointing away from the NAM ligands (Fig. 7). Yet, several mutations of this residue produced substantial changes in potency for all three NAMs (Fig. 5 and 7). V514 is located in the pre-M1 helix of the linker, and this residue potentially has a critical role for the stability or position of this structural element. The pre-M1 helix is part of the NAM pocket, and several residues in the pre-M1 helix make direct contacts to the NAMs. Thus, the results for V514 are likely an example of how point-mutations can affect ligand potencies via indirect allosteric effects on ligand binding pockets.

Key interactions that were previously suggested from the GluA2/NAM crystal structures and mutational analysis by Yelshanskaya *et al.* (2016) are supported by our mutational data and models. These include hydrogen bonding interactions involving N791, and hydrophobic and  $\pi$ -stacking interactions involving P520 and F623 (Fig. 8 and 9). In contrast, the idea of key HB interactions of the side chains of S788 and Y616 with all of the tested NAMs is not supported by our mutational data or modeling. Specifically, in our modeling we only observe an HB interaction between Y616 and GYKI. However, the Y616F mutation did not change GYKI potency and therefore did not support the presence of this interaction (Fig. 7). S615 has also been suggested to form HBs to the NAM ligands, and mutation to Ala was previously reported to cause an order of magnitude loss of potency for GYKI and PMP (Yelshanskaya et al., 2016). When desensitization was blocked by CTZ in the  $[Ca^{2+}]_i$  assay and in TEVC experiments (similar to the patch-clamp electrophysiology experiments by Yelshanskaya *et al.*), we observed similar loss-of-potency effects by the S615A mutation, while CP potency remained unchanged (Fig. 7 and Supplemental Fig. S3). However, in TEVC experiments without CTZ, S615A did not change potency for PMP and GYKI, but increased potency of CP by an order of magnitude. These results suggest that the role of S615 in NAM binding is state-dependent; e.g. that block of desensitization by CTZ causes a different

**MOL # 116871**

conformation of S615 compared to the receptor population in our TEVC experiments without CTZ in which the vast majority of receptors are desensitized. Interestingly, the S615A mutant has been previously reported to display slower rates of deactivation and desensitization and an increased fraction of steady-state to peak current (Yelshanskaya et al., 2017). Several other mutants display differential effects on NAM potencies between assays, albeit not to the same extent as the S615A mutant. Possibly, other residues in the NAM binding region play state-dependent roles in NAM inhibition due to state-dependent variations in their structural conformations or mutational effects on receptor desensitization as reported for several residues in the region (Yelshanskaya et al., 2017). This aspect of NAM molecular pharmacology is of potential interest as AMPAR activation and desensitization are thought to involve transitions between multiple open and desensitized states (Jin et al., 2003; Robert and Howe, 2003; Robert et al., 2001). Also, the receptor activation mechanism may involve multiple pre-activated states (Durr et al., 2014). The dependence of NAM binding on different receptor conformations underlying this potential multitude of functional states and which state transitions are affected by NAM binding is at present unknown. Concerning this, it is interesting to note early observations (Johansen et al., 1995) that NAM potency appears to be affected by PAM ligands that now are known to bind in the LBD dimer interfaces and stabilize non-desensitized conformations of the LBD layer. Interestingly, our results indicate that the interactions of specific AMPAR residues with the NAMs can be altered by the presence of PAMs. Future modeling studies, potentially involving molecular dynamics simulations, aiming to compare the configuration of the NAM binding site in AMPAR structures representing different functional states seem warranted. In addition, inclusion of a lipid bilayer in the models may likely provide additional insight into how membrane lipids influence the NAM binding pocket. Such studies may reveal potentially important effects of the presence of different types of lipids on side chain orientation of residues such as V514 that in our models appears to orientate towards the membrane. Furthermore, an important open question to answer will be the role of co-operability of the four NAM sites per receptor complex; including the number of sites needed to be occupied to achieve inhibition of channel gating. Moreover, auxiliary subunits also influence AMPAR states and transitions; adding a layer of complexity to understanding the structural basis of AMPAR function (Dawe et al., 2016; Greger et al., 2017). In this relation, it is interesting to note that novel classes of NAMs have recently been reported that modulate AMPARs depending on the presence of certain members of the TARP family (Azumaya et al., 2017; Gardinier et al., 2016; Maher et al., 2016).

In summary, we have performed mutational analysis and modeling of the NAM binding pockets and ligand binding modes in the GluA2 AMPAR that in combination with recent X-ray crystal structures published by others (Yelshanskaya et al., 2016) constitute a step toward achieving a full molecular understanding of this important class of AMPAR inhibitors.

MOL # 116871

### **9. Authorship Contributions**

*Participated in research design:* Stenum-Berg, Musgaard, Chavez-Abiega, Biggin, and Kristensen.

*Conducted experiments:* Stenum-Berg, Musgaard, Chavez-Abiega, Thisted, and Barella.

*Contributed new reagents or analytic tools:* Musgaard and Biggin.

*Performed data analysis:* Stenum-Berg, Musgaard, Chavez-Abiega, Thisted, Barella, and Kristensen.

*Wrote or contributed to the writing of the manuscript:* Stenum-Berg, Musgaard, Biggin, and Kristensen

## 10. References

- Azumaya CM, Days EL, Vinson PN, Stauffer S, Sulikowski G, Weaver CD and Nakagawa T (2017) Screening for AMPA receptor auxiliary subunit specific modulators. *PLoS one* **12**(3): e0174742.
- Balannik V, Menniti FS, Paternain AV, Lerma J and Stern-Bach Y (2005) Molecular mechanism of AMPA receptor noncompetitive antagonism. *Neuron* **48**(2): 279-288.
- Berman HM, Westbrook J, Feng Z, Gilliland G, Bhat TN, Weissig H, Shindyalov IN and Bourne PE (2000) The Protein Data Bank. *Nucleic acids research* **28**(1): 235-242.
- Chen S, Zhao Y, Wang Y, Shekhar M, Tajkhorshid E and Gouaux E (2017) Activation and Desensitization Mechanism of AMPA Receptor-TARP Complex by Cryo-EM. *Cell* **170**(6): 1234-1246 e1214.
- Chinea G, Padron G, Hooft RW, Sander C and Vriend G (1995) The use of position-specific rotamers in model building by homology. *Proteins* **23**(3): 415-421.
- Citraro R, Aiello R, Franco V, De Sarro G and Russo E (2014) Targeting alpha-amino-3-hydroxy-5-methyl-4-isoxazole-propionate receptors in epilepsy. *Expert opinion on therapeutic targets* **18**(3): 319-334.
- Cokic B and Stein V (2008) Stargazin modulates AMPA receptor antagonism. *Neuropharmacology* **54**(7): 1062-1070.
- Dawe GB, Musgaard M, Aurousseau MRP, Nayeem N, Green T, Biggin PC and Bowie D (2016) Distinct Structural Pathways Coordinate the Activation of AMPA Receptor-Auxiliary Subunit Complexes. *Neuron* **89**(6): 1264-1276.
- Di Bonaventura C, Labate A, Maschio M, Meletti S and Russo E (2017) AMPA receptors and perampanel behind selected epilepsies: current evidence and future perspectives. *Expert opinion on pharmacotherapy* **18**(16): 1751-1764.
- Durr KL, Chen L, Stein RA, De Zorzi R, Folea IM, Walz T, McHaourab HS and Gouaux E (2014) Structure and Dynamics of AMPA Receptor GluA2 in Resting, Pre-Open, and Desensitized States. *Cell*.
- Gardinier KM, Gernert DL, Porter WJ, Reel JK, Ornstein PL, Spinazze P, Stevens FC, Hahn P, Hollinshead SP, Mayhugh D, Schkeryantz J, Khilevich A, De Frutos O, Gleason SD, Kato AS, Luffer-Atlas D, Desai PV, Swanson S, Burris KD, Ding C, Heinz BA, Need AB, Barth VN, Stephenson GA, Diserod BA, Woods TA, Yu H, Bredt D and Witkin JM (2016) Discovery of the First alpha-Amino-3-hydroxy-5-methyl-4-isoxazolepropionic Acid (AMPA) Receptor Antagonist Dependent upon Transmembrane AMPA Receptor Regulatory Protein (TARP) gamma-8. *Journal of medicinal chemistry* **59**(10): 4753-4768.
- Greger IH, Watson JF and Cull-Candy SG (2017) Structural and Functional Architecture of AMPA-Type Glutamate Receptors and Their Auxiliary Proteins. *Neuron* **94**(4): 713-730.
- Haering SC, Tapken D, Pahl S and Hollmann M (2014) Auxiliary subunits: shepherding AMPA receptors to the plasma membrane. *Membranes* **4**(3): 469-490.
- Hanada T (2014) The discovery and development of perampanel for the treatment of epilepsy. *Expert opinion on drug discovery* **9**(4): 449-458.
- Hanada T, Hashizume Y, Tokuhara N, Takenaka O, Kohmura N, Ogasawara A, Hatakeyama S, Ohgoh M, Ueno M and Nishizawa Y (2011) Perampanel: a novel, orally active, noncompetitive AMPA-receptor antagonist that reduces seizure activity in rodent models of epilepsy. *Epilepsia* **52**(7): 1331-1340.
- Herguedas B, Watson JF, Ho H, Cais O, Garcia-Nafria J and Greger IH (2019) Architecture of the heteromeric GluA1/2 AMPA receptor in complex with the auxiliary subunit TARP gamma8. *Science* **364**(6438).
- Humphrey W, Dalke A and Schulten K (1996) VMD: visual molecular dynamics. *Journal of molecular graphics* **14**(1): 33-38, 27-38.
- Jackson AC and Nicoll RA (2011) The expanding social network of ionotropic glutamate receptors: TARPs and other transmembrane auxiliary subunits. *Neuron* **70**(2): 178-199.
- Jespersen T, Grunnet M, Angelo K, Klaerke DA and Olesen SP (2002) Dual-function vector for protein expression in both mammalian cells and *Xenopus laevis* oocytes. *BioTechniques* **32**(3): 536-538, 540.
- Jin R, Banke TG, Mayer ML, Traynelis SF and Gouaux E (2003) Structural basis for partial agonist action at ionotropic glutamate receptors. *Nature neuroscience* **6**(8): 803-810.
- Johansen TH, Chaudhary A and Verdoorn TA (1995) Interactions among GYKI-52466, cyclothiazide, and aniracetam at recombinant AMPA and kainate receptors. *Molecular pharmacology* **48**(5): 946-955.
- Karakas E, Regan MC and Furukawa H (2015) Emerging structural insights into the function of ionotropic glutamate receptors. *Trends Biochem Sci* **40**(6): 328-337.
- Kessels HW and Malinow R (2009) Synaptic AMPA receptor plasticity and behavior. *Neuron* **61**(3): 340-350.
- Kumar J and Mayer ML (2013) Functional Insights from Glutamate Receptor Ion Channel Structures. *Annu Rev Physiol* **75**: 313-337.
- Lam VM, Beerepoot P, Angers S and Salahpour A (2013) A Novel Assay for Measurement of Membrane-Protein Surface Expression using a beta-lactamase Reporter. *Traffic* **14**(7): 778-784.
- Lazzaro JT, Paternain AV, Lerma J, Chenard BL, Ewing FE, Huang J, Welch WM, Ganong AH and Menniti FS (2002) Functional characterization of CP-465,022, a selective, noncompetitive AMPA receptor antagonist. *Neuropharmacology* **42**(2): 143-153.
- Liman ER, Tytgat J and Hess P (1992) Subunit stoichiometry of a mammalian K<sup>+</sup> channel determined by construction of multimeric cDNAs. *Neuron* **9**(5): 861-871.
- Lindorff-Larsen K, Piana S, Palmo K, Maragakis P, Klepeis JL, Dror RO and Shaw DE (2010) Improved side-chain torsion potentials for the Amber ff99SB protein force field. *Proteins-Structure Function and Bioinformatics* **78**(8): 1950-1958.

MOL # 116871

- Maher MP, Wu N, Ravula S, Ameriks MK, Savall BM, Liu C, Lord B, Wyatt RM, Matta JA, Dugovic C, Yun S, Ver Donck L, Steckler T, Wickenden AD, Carruthers NI and Lovenberg TW (2016) Discovery and Characterization of AMPA Receptor Modulators Selective for TARP-gamma8. *The Journal of pharmacology and experimental therapeutics* **357**(2): 394-414.
- Menniti FS, Chenard BL, Collins MB, Ducat MF, Elliott ML, Ewing FE, Huang JI, Kelly KA, Lazzaro JT, Pagnozzi MJ, Weeks JL, Welch WM and White WF (2000) Characterization of the binding site for a novel class of noncompetitive alpha-amino-3-hydroxy-5-methyl-4-isoxazolepropionic acid receptor antagonists. *Molecular pharmacology* **58**(6): 1310-1317.
- Micale N, Colleoni S, Postorino G, Pellicano A, Zappala M, Lazzaro J, Diana V, Cagnotto A, Mennini T and Grasso S (2008) Structure-activity study of 2,3-benzodiazepin-4-ones noncompetitive AMPAR antagonists: identification of the 1-(4-amino-3-methylphenyl)-3,5-dihydro-7,8-ethylenedioxy-4H-2,3-benzodiazepin-4-one as neuroprotective agent. *Bioorganic & medicinal chemistry* **16**(5): 2200-2211.
- Mittapalli GK and Roberts E (2014) Structure activity relationships of novel antiepileptic drugs. *Current medicinal chemistry* **21**(6): 722-754.
- Moncada C, Arvin B, Le Peillet E and Meldrum BS (1991) Non-NMDA antagonists protect against kainate more than AMPA toxicity in the rat hippocampus. *Neuroscience letters* **133**(2): 287-290.
- Poulsen MH, Lucas S, Bach TB, Barslund AF, Wenzler C, Jensen CB, Kristensen AS and Stromgaard K (2013) Structure-activity relationship studies of argiotoxins: selective and potent inhibitors of ionotropic glutamate receptors. *Journal of medicinal chemistry* **56**(3): 1171-1181.
- Robert A and Howe JR (2003) How AMPA receptor desensitization depends on receptor occupancy. *The Journal of neuroscience : the official journal of the Society for Neuroscience* **23**(3): 847-858.
- Robert A, Irizarry SN, Hughes TE and Howe JR (2001) Subunit interactions and AMPA receptor desensitization. *The Journal of neuroscience : the official journal of the Society for Neuroscience* **21**(15): 5574-5586.
- Sali A and Blundell TL (1993) Comparative protein modelling by satisfaction of spatial restraints. *Journal of molecular biology* **234**(3): 779-815.
- Salomon-Ferrer R, Case DA and Walker RC (2013) An overview of the Amber biomolecular simulation package. *Wires Comput Mol Sci* **3**(2): 198-210.
- Sobolevsky AI, Rosconi MP and Gouaux E (2009) X-ray structure, symmetry and mechanism of an AMPA-subtype glutamate receptor. *Nature* **462**(7274): 745-756.
- Solyom S and Tarnawa I (2002) Non-competitive AMPA antagonists of 2,3-benzodiazepine type. *Current pharmaceutical design* **8**(10): 913-939.
- Sorensen L, Stromgaard K and Kristensen AS (2014) Characterization of intracellular regions in the human serotonin transporter for phosphorylation sites. *ACS chemical biology* **9**(4): 935-944.
- Sousa da Silva AW and Vranken WF (2012) ACPYPE - AnteChamber PYthon Parser interface. *BMC research notes* **5**: 367.
- Sun Y, Olson R, Horning M, Armstrong N, Mayer M and Gouaux E (2002) Mechanism of glutamate receptor desensitization. *Nature* **417**(6886): 245-253.
- Traynelis SF, Wollmuth LP, McBain CJ, Menniti FS, Vance KM, Ogden KK, Hansen KB, Yuan H, Myers SJ and Dingledine R (2010) Glutamate receptor ion channels: structure, regulation, and function. *Pharmacological reviews* **62**(3): 405-496.
- Trott O and Olson AJ (2010) AutoDock Vina: improving the speed and accuracy of docking with a new scoring function, efficient optimization, and multithreading. *Journal of computational chemistry* **31**(2): 455-461.
- Twomey EC and Sobolevsky AI (2018) Structural Mechanisms of Gating in Ionotropic Glutamate Receptors. *Biochemistry* **57**(3): 267-276.
- Twomey EC, Yelshanskaya MV, Grassucci RA, Frank J and Sobolevsky AI (2016) Elucidation of AMPA receptor-stargazin complexes by cryo-electron microscopy. *Science* **353**(6294): 83-86.
- Twomey EC, Yelshanskaya MV, Grassucci RA, Frank J and Sobolevsky AI (2017a) Channel opening and gating mechanism in AMPA-subtype glutamate receptors. *Nature* **549**(7670): 60-65.
- Twomey EC, Yelshanskaya MV, Grassucci RA, Frank J and Sobolevsky AI (2017b) Structural Bases of Desensitization in AMPA Receptor-Auxiliary Subunit Complexes. *Neuron* **94**(3): 569-580 e565.
- Van der Spoel D, Lindahl E, Hess B, Groenhof G, Mark AE and Berendsen HJC (2005) GROMACS: Fast, flexible, and free. *Journal of computational chemistry* **26**(16): 1701-1718.
- Vriend G (1990) WHAT IF: a molecular modeling and drug design program. *Journal of molecular graphics* **8**(1): 52-56, 29.
- Wang J, Wolf RM, Caldwell JW, Kollman PA and Case DA (2004) Development and testing of a general amber force field. *Journal of computational chemistry* **25**(9): 1157-1174.
- Yelshanskaya MV, Li M and Sobolevsky AI (2014) Structure of an agonist-bound ionotropic glutamate receptor. *Science*.
- Yelshanskaya MV, Mesbahi-Vasey S, Kurnikova MG and Sobolevsky AI (2017) Role of the Ion Channel Extracellular Collar in AMPA Receptor Gating. *Scientific reports* **7**(1): 1050.
- Yelshanskaya MV, Singh AK, Sampson JM, Narangoda C, Kurnikova M and Sobolevsky AI (2016) Structural Bases of Noncompetitive Inhibition of AMPA-Subtype Ionotropic Glutamate Receptors by Antiepileptic Drugs. *Neuron* **91**(6): 1305-1315.
- Zarate CA, Jr. and Manji HK (2008) The role of AMPA receptor modulation in the treatment of neuropsychiatric diseases. *Experimental neurology* **211**(1): 7-10.

**MOL # 116871**

- Zhao Y, Chen S, Swensen AC, Qian WJ and Gouaux E (2019) Architecture and subunit arrangement of native AMPA receptors elucidated by cryo-EM. *Science* **364**(6438): 355-362.
- Zhu S and Gouaux E (2017) Structure and symmetry inform gating principles of ionotropic glutamate receptors. *Neuropharmacology* **112**(Pt A): 11-15.
- Zwart R, Sher E, Ping X, Jin X, Sims JR, Chappell AS, Gleason SD, Hahn PJ, Gardinier K, Gernert D, Hobbs J, Smith JL, Valli SN and Witkin JM (2014) Perampanel, an Antagonist of alpha-amino-3-hydroxy-5-methyl-4-isoxazolepropionic acid (AMPA) Receptors for the Treatment of Epilepsy: Studies in Human Epileptic Brain, Non-Epileptic Brain, and in Rodent Models. *The Journal of pharmacology and experimental therapeutics*.

11. Tables

**Table 1.** Effect of mutations on GluA2  $EC_{50}$  and  $E_{max}$  for glutamate.

Construct	$E_{max}$ (% of WT)	$EC_{50}^a$ ( $\mu$ M)	
	$[Ca^{2+}]_i$	$[Ca^{2+}]_i$	TEVC
GluA2	100	17 [16-17]**	23 [23-23]
<i>blac</i> -GluA2	102 [82-121]	14 [14-15]	27 [27-28]
K511G	29 [22-36]***	4.3 [4.0-4.6]**	30 [30-31]*
P512G	134 [91-177]	27 [26-29]**	43 [42-44]**
V514G	28 [21-35]***	11 [9.6-13]**	26 [25-27]
V514A	36 [17-56]**	5.7 [3.4-9.6]**	12 [12-12]**
V514D	76 [24-128]	3.7 [2.2-6.3]**	29 [28-30]
V514W	63 [42-84]	7.5 [6.6-8.6]**	32 [31-32]*
F515G	86 [61-112]	38 [37-39]**	35 [34-36]*
F515A	135 [-16-286]	12 [9.2-15]	N.D.
S516G	99 [91-107]	29 [27-32]**	N.D.
F517G	38 [32-44]***	130 [130-140]***	N.D.
F517A	54 [50-57]*	70 [66-75]***	N.D.
L518G	N.F.	N.F.	N.D.
L518A	61 [48-74]	89 [82-97]***	31 [30-32]*
D519G	63 [41-86]	8.9 [8.0-9.8]**	N.D.
D519N	91 [81-101]	14 [14-15]	37 [37-38]**
P520G	N.F.	N.F.	N.D.
L521G	N.F.	N.F.	N.D.
L521A	N.F.	N.F.	N.D.
A522G	99 [83-114]	20 [19-23]**	N.D.
A522S	63 [47-80]*	13 [12-13]	N.D.
Y523G	93 [73-113]	28 [26-30]**	N.D.
Y523P	87 [81-94]	12 [12-13]	N.D.
Y523R	99 [85-114]	19 [18-20]*	N.D.
E524G	60 [56-65]*	36 [34-38]**	N.D.
E524D	47 [23-71]***	19 [17-21]*	37 [37-38]**
I525G	N.F.	N.F.	N.D.
W526G	N.F.	N.F.	N.D.
M527G	99 [87-111]	27 [25-30]**	N.D.
S615A	68 [-50-187]	2.5 [0.7-8.5]*	22 [22-23]**
Y616F	N.F.	N.F.	26 [26-26]
F623A	65 [39-91]	90 [79-100]***	16 [16-17]**
E782G	104 [87-120]	33 [31-35]**	N.D.
K783G	112 [100-125]	11 [10-12]**	N.D.
T784G	143 [69-217]	47 [46-49]***	26 [26-27]
S785G	124 [108-140]	49 [46-51]***	25 [25-26]
A786G	100 [67-134]	82 [80-84]***	36 [34-38]**
L787G	N.F.	N.F.	N.D.

MOL # 116871

Table 1 continued

S788G	111 [93-129]	36 [34-39]**	N.D.
L789G	31 [16-47]***	55 [52-58]***	N.D.
S790G	99 [73-125]	21 [19-22]*	N.D.
N791G	90 [76-105]	24 [22-25]**	N.D.
N791A	65 [23-108]	6.0 [5.0-7.2]**	20 [19-21]**
N791F	38 [27-49]***	200 [190-210]***	N.D.
N791L	32 [22-43]***	8.9 [7.5-10]*	N.D.
V792G	N.F.	N.F.	N.D.
V792I	77 [53-102]	14 [13-16]	33 [32-33]**
A793G	81 [69-92]	24 [23-26]**	N.D.
A793D	49 [36-62]**	2.4 [2.1-2.8]**	N.D.
A793H	69 [51-88]	13 [12-14]	N.D.
G794D	64 [49-79]	5.2 [4.6-5.7]**	50 [49-50]***
G794H	N.F.	N.F.	N.D.
V795G	72 [48-96]	32 [30-35]**	N.D.
F796G	N.F.	N.F.	N.D.
Y797G	N.F.	N.F.	N.D.

<sup>a</sup>  $EC_{50}$  values were determined by the nonlinear fitting of composite concentration-inhibition data from at least three independent experiments (TEVC or  $Ca^{2+}$ ) (see *Materials and Methods*). Numbers in parentheses denote the 95% confidence interval. \*,  $p < 0.05$ ; \*\*,  $p < 0.01$ ; \*\*\*,  $p < 0.001$  significantly different from *blac*-GluA2 (ANOVA). To maintain an overall familywise alpha of 5%, for each dependent variable separate ANOVA with Dunnett's post hoc test were run at  $\alpha = 0.05/dv$ , where  $dv$  is the number of dependent variables.

MOL # 116871

**Table 2.**  $IC_{50}$  values for PMP, CP, and GYKI at WT and mutant GluA2.

Construct	PMP		CP		GYKI	
	$[Ca^{2+}]_i$	TEVC	$[Ca^{2+}]_i$	TEVC	$[Ca^{2+}]_i$	TEVC
GluA2	29 [28-29]***	4.3 [4.2-4.4]***	2.5 [2.5-2.6]**	2.5 [2.4-2.6]	230 [230-230]***	20 [19-21]
<i>blac</i> -GluA2	16 [15-18]	2.4 [2.3-2.5]	1.1 [1.0-1.2]	2.4 [2.3-2.6]	120 [110-120]	25 [25-26]
K511G	>100***	9.6 [9.3-9.9]***	9.3 [7.0-12]***	3.3 [3.1-3.4]	>2000***	62 [49-78]***
P512G	9.8 [8.4-11]*	4.4 [4.3-4.5]***	5.5 [5.0-6.0]***	7.5 [7.2-7.8]***	140 [100-180]	79 [75-84]***
V514G	>100***	29 [26-31]***	>100***	10 [9.6-10]***	>2000***	620 [450-850]***
V514A	>100***	4.7 [4.4-4.9]***	27 [23-31]***	3.3 [3.1-3.6]	>2000***	11 [10-12]***
V514D	19 [14-26]	11 [11-11]***	6.0 [5.8-6.3]***	4.0 [3.8-4.3]	>2000***	69 [66-73]***
V514W	87 [71-110]***	2.3 [2.3-2.4]	4.2 [3.7-4.7]***	0.9 [0.9-1.0]***	>2000***	18 [18-19]
F515G	4.1 [3.7-4.5]***	1.6 [1.6-1.6]***	0.7 [0.7-0.8]	1.6 [1.6-1.7]	20 [19-21]***	7.9 [7.7-8.1]***
F515A	4.5 [3.7-5.6]***	-	0.4 [0.4-0.4]**	-	49 [42-57]***	-
S516G	23 [19-27]	-	3.5 [3.3-3.8]***	-	670 [520-860]***	-
F517G	1.0 [1.0-1.1]***	-	0.3 [0.3-0.3]***	-	13 [12-13]***	-
F517A	4.9 [4.6-5.2]***	-	2.4 [2.1-2.6]	-	53 [47-58]***	-
L518A	2.9 [2.5-3.2]***	3.8 [3.7-3.9]***	0.8 [0.8-0.8]	1.9 [1.8-1.9]	28 [27-30]***	28 [27-29]
D519G	10 [9.2-11]**	-	3.7 [3.4-4.0]***	-	19 [17-20]***	-
D519N	24 [17-34]	3.3 [3.2-3.5]***	61 [18-210]***	7.4 [7.0-7.8]***	55 [47-63]***	8.1 [7.7-8.5]***
A522G	17 [14-20]	-	1.7 [1.6-1.8]	-	310 [280-350]***	-
A522S	16 [14-18]	-	2.4 [2.2-2.7]	-	510 [400-650]***	-
Y523G	12 [10-14]	-	1.2 [1.2-1.3]	-	91 [77-1107]	-
Y523P	18 [12-27]	-	3.1 [2.8-3.4]**	-	370 [320-430]***	-
Y523R	15 [13-17]	-	1.8 [1.6-1.9]	-	84 [76-93]*	-
E524G	9.5 [8.7-10]***	-	0.5 [0.5-0.5]*	-	48 [43-52]***	-
E524D	23 [19-27]	2.0 [1.9-2.1]***	5.0 [3.9-6.4]***	1.6 [1.5-1.6]	140 [110-180]	14 [14-15]**
M527G	8.9 [7.9-10]**	-	0.5 [0.4-0.6]	-	120 [100-140]	-
S615A	>100***	2.2 [2.1-2.3]	3.5 [3.3-3.7]*	0.2 [0.2-0.2]***	>2000***	31 [14-66]
Y616F	-	0.9 [0.5-1.7]***	-	1.8 [1.6-1.9]	-	26 [15-46]

MOL # 116871

Table 2 continued

F623A	>100***	>100***	12 [7.2-21]***	51 [4.4-590]***	100 [88-120]	87 [35-210]***
E782G	12 [11-13]	-	1.1 [1.1-1.2]	-	100 [97-110]	-
K783G	27 [19-39]**	-	2.7 [2.6-2.8]*	-	170 [160-180]**	-
T784G	8.5 [7.3-9.8]***	7.9 [7.6-8.2]***	1.1 [1.0-1.2]	2.5 [2.5-2.5]	23 [21-25]***	22 [22-23]
S785G	10 [9.0-11]**	3.5 [3.4-3.7]***	1.1 [1.0-1.2]	1.7 [1.6-1.7]	39 [36-42]***	12 [12-12]***
A786G	1.4 [1.3-1.6]***	2.7 [2.6-2.7]**	0.6 [0.5-0.6]	3.1 [3.0-3.2]	18 [17-19]***	11 [11-12]***
L787A	37 [18-74]***	-	7.1 [6.6-7.6]***	-	630 [500-780]***	-
S788G	16 [14-18]	-	0.6 [0.6-0.6]	-	92 [77-110]	-
L789G	4.8 [4.3-5.4]***	-	0.4 [0.3-0.4]***	-	61 [51-73]***	-
S790G	9.9 [5.4-18]*	-	1.5 [1.4-1.7]	-	140 [100-180]	-
N791G	8.7 [6.4-12]***	-	15 [9.2-24]***	-	350 [300-420]***	-
N791A	>100***	1.5 [1.5-1.6]***	>100***	11 [10-13]***	>2000***	21 [21-22]
N791F	3.7 [3.5-3.8]***	-	1.9 [1.9-2.0]	-	22 [20-23]***	-
N791L	14 [13-15]	-	25 [19-33]***	-	66 [62-69]***	-
V792I	14 [12-16]	1.2 [1.2-1.3]***	13 [9.2-17]***	2.1 [2.0-2.2]	170 [140-200]*	11 [10-11]***
A793G	12 [8.9-17]	-	1.1 [1.0-1.2]	-	180 [150-220]***	-
A793D	27 [18-41]**	-	170 [8.6-3500]***	-	190 [170-200]***	-
A793H	15 [12-18]	-	3.7 [3.0-4.5]***	-	110 [110-120]	-
G794D	37 [30-46]***	5.5 [5.4-5.7]***	11 [8.4-14]***	2.8 [2.7-2.9]	280 [250-310]***	40 [39-41]*
V795G	15 [10-21]	-	1.1 [0.9-1.2]	-	87 [74-100]	-

<sup>a</sup>  $IC_{50}$  values were determined by the nonlinear fitting of composite concentration-inhibition data from at least three independent experiments (TEVC or  $Ca^{2+}$ ) (see *Materials and Methods*). Numbers in parentheses denote the 95% confidence interval for the fitted  $IC_{50}$ . \*,  $p < 0.05$ ; \*\*,  $p < 0.01$ ; \*\*\*,  $p < 0.001$  significantly different from *blac*-GluA2 (ANOVA). To maintain an overall familywise alpha of 5%, for each dependent variable separate ANOVA with Dunnett's post hoc test were run at  $\alpha = 0.05/dv$ , where  $dv$  is the number of dependent variables.

### 10. Figure legends

**Figure 1. Structure of the GluA2 AMPAR (PDB 3KG2) and the negative allosteric modulators. (A)** Cartoon representation of the structure of the GluA2 receptor with indications of the major domain regions (ATD, LBD, and TMD). The LBD-TMD linker region is located in the rectangular box, which shows an expanded view of the linker region of a single subunit (*light blue*) including the M3 helix of a neighboring subunit (*gray*). Residue positions previously reported to affect NAM selectivity and/or potency are highlighted in yellow. **(B)** Chemical structures of the NAMs perampanel, CP-465,022, and GYKI-53,655.

**Figure 2. Characterization of WT and mutant *blac*-GluA2 function in HEK cells using a 96-well based  $[Ca^{2+}]$  imaging assay. (A)** Representative traces from recordings of  $Ca^{2+}$  dye fluorescence from HEK293 cells transfected with WT and mutant *blac*-GluA2 receptors with the application of increasing Glu concentrations. F517G and I525G exemplify mutants with medium or no response, respectively, to Glu application. Traces represent mean fluorescence from four identical wells. **(B)** Representative examples of Glu concentration-response curves for WT, a loss-of-potency mutant (F517G), a gain-of-potency mutant (K511G), and a WT-like mutant (D519G). Data points represent the mean from 3 independent concentration-response experiments (*Materials & Methods*). Error bars are the SD and are shown when larger than symbol size.

**Figure 3. Summary of functional characterization of Gly mutants of GluA2. (A)** Overview of positions in GluA2 subjected to Gly-substitution in the four segments of the LBD-TMD linker region of a single GluA2 subunit (S1-M1 linker, upper M1, S2-M4 linker, and upper M4; shown as cartoon representation in blue). M3 of the neighboring subunit is shown in gray cartoon representation. Mutated positions are shown as green spheres. Dark gray spheres indicate positions where Gly-substitution rendered GluA2 non-functional. **(B-C)** Graphical summary of the fold-change in Glu potency ( $EC_{50}$ ) and maximal response amplitude ( $E_{max}$ ) for mutants relative to WT *blac*-GluA2 measured by  $[Ca^{2+}]_i$  imaging. Fold-change values for  $EC_{50}$  are calculated from values in Table 1 as  $EC_{50(WT)}/EC_{50(mutant)}$  for mutants displaying decreased  $EC_{50}$  and as  $EC_{50(mutant)}/EC_{50(WT)}$  for mutants displaying increased  $EC_{50}$ . The light gray shaded area indicates mutants with fold changes less than three-fold compared to WT. The dark gray area indicates non-functional mutants. Filled gray circles indicate mutants that were statistically different from WT *blac*-GluA2 and white circles indicate mutants that were not statistically different from WT *blac*-GluA2 (see Table 1).

**Figure 4. Determination of NAM inhibitory potency at WT and mutant *blac*-GluA2 function in HEK cells. (A-C)** Representative traces illustrating the effect of increasing concentrations of a NAM (PMP) on increases in  $Ca^{2+}$  dye fluorescence upon application of Glu (*indicated by arrow*) in HEK293 cells transfected with WT and

MOL # 116871

mutant *blac*-GluA2 receptors. V514G (B) and F517G (C) exemplify mutants that display NAM loss-of-potency (V514G) or gain-of-potency (F517G), respectively. All traces are normalized to the maximum fluorescence without NAM and represent the mean fluorescence from four identical wells. (D-F) Concentration inhibition curves for PMP at WT and mutant *blac*-GluA2 illustrating examples of mutants where PMP displays unchanged potency (P512G, D), loss-of-potency (V514G, E), and gain-of-potency (F517G, F). Data points represent the mean from three independent concentration-response experiments (*Materials & Methods*). Error bars are the SD and are shown when larger than symbol size.

**Figure 5. Summary of NAM inhibitory potencies at Gly mutants of *blac*-GluA2.** (A) Overview of the positions in GluA2 that were subjected to Gly-substitution in four segments of the LBD-TMD linker region (S1-M1 linker and upper M1 in the upper panel, S2-M4 linker and upper M4 in lower panel). Color coding as in Figure 3. (B) Graphical summary of the fold-change in  $IC_{50}$  of PMP (*left*), CP (*middle*), and GYKI (*right*) for mutants relative to WT *blac*-GluA2 measured by  $[Ca^{2+}]_i$  imaging. Fold-change values for  $IC_{50}$  are calculated from values in Table 2 as  $IC_{50(WT)}/IC_{50(mutant)}$  for mutants displaying decreased  $IC_{50}$  and as  $IC_{50(mutant)}/IC_{50(WT)}$  for mutants displaying increased  $IC_{50}$ . White circles indicate mutants that were not statistically different from WT *blac*-GluA2, and colored circles indicate mutants that were statistically different from WT *blac*-GluA2 (see Table 1), with mutants displaying no or less than five-fold changes indicated with gray circles, mutants displaying more than five-fold increase (loss-of-potency) indicated in red, and mutants displaying more than five-fold decrease (gain-of-potency) in green.

**Figure 6. TEVC characterization of WT and mutant *blac*-GluA2 receptors.** (A-B) Representative current traces illustrate the recording protocol used for concentration-response experiments for determination of Glu  $EC_{50}$  (A) and inhibitor  $IC_{50}$  (B) at WT (*upper traces*) and a representative mutant (V514G; *lower traces*) *blac*-GluA2 receptors expressed in *Xenopus* oocytes (*Materials and methods*). (C-D) Average composite concentration-response curves from 4 to 8 oocytes. Error bars are the SD and are shown when larger than symbol size. The current responses are normalized to the maximal response produced by Glu (1 mM).

**Figure 7. Summary of effects on NAM inhibitory potency of non-Gly mutations in *blac*-GluA2.** (A) Combined cartoon and stick representation of a single NAM binding site from the GluA2/NAM X-ray crystal structures (PDB 5L1F for PMP, PDB 5L1E for CP, and PDB 5L1H for GYKI) as determined by Yelshanskaya et al. (2016). Ligand positions and orientation of NAM structures are shown for PMP (*left, yellow*), CP (*middle, orange*), and GYKI (*right, magenta*). Residue positions subjected to non-Gly mutations are shown as green sticks. (B) Graphical summary of the fold-change in  $IC_{50}$  measured by  $[Ca^{2+}]_i$  imaging of PMP (*left*), CP

MOL # 116871

(*middle*), and GYKI (*right*) for mutants relative to WT *blac*-GluA2. Fold-change is calculated from  $IC_{50}$  values in Table 2 as  $IC_{50}(WT)/IC_{50}(\text{mutant})$  for mutants displaying decreased  $IC_{50}$  and as  $IC_{50}(\text{mutant})/IC_{50}(WT)$  for mutants displaying increased  $IC_{50}$ . White circles indicate mutants that were not statistically different from WT *blac*-GluA2, and filled circles indicate mutants that were statistically different from WT *blac*-GluA2 (See Table 2), with mutants displaying no or less than five-fold changes indicated with gray circles, mutants displaying more than five-fold increase (loss-of-potency) indicated in *red*, and mutants displaying more than five-fold decrease (gain-of-potency) in green.

**Figure 8. Variability in side chain conformations among models of the GluA2 NAM binding pocket. (A-C)**

Overlay of 50 models for each GluA2 NAM binding site with residues within 5 Å shown as lines, with hydrophobic residues in gray and hydrophilic residues in green. Each panel shows zoom-ins on the NAM binding pocket harboring PMP (A, *yellow*), CP (B, *orange*) and GYKI (C, *magenta*).

**Figure 9. Representative models of the GluA2 NAM binding pocket. (A-C)**

Models of the NAM binding pocket harboring PMP (A, *yellow*), CP (B, *orange*) and GYKI (C, *magenta*). Representations of the secondary structure elements of a single subunit surrounding the ligand (*green*) and the M3 helix of a neighboring subunit (*gray*). Residues in the vicinity of the NAMs are shown as sticks with hydrophobic residues highlighted in gray and hydrophilic residues in green. Potential HBs are indicated as dashed lines.

MOL # 116871

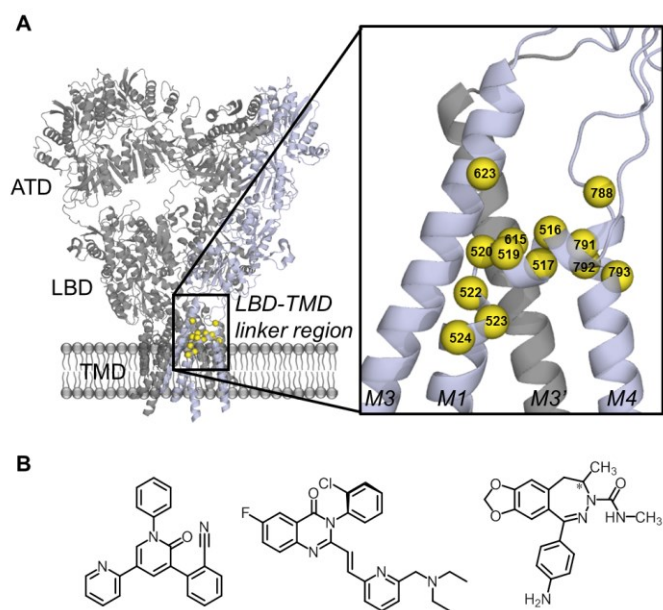
### ***11. Footnotes***

This work was supported by The Danish Council for Independent Research [grants to A.S.K.], and the Faculty of Health and Medical Science, University of Copenhagen [PhD stipend to CSB]. MM was supported by a postdoctoral fellowship from the Alfred Benzon Foundation. We thank Alexander B. J. Jensen for excellent technical assistance.

MOL # 116871

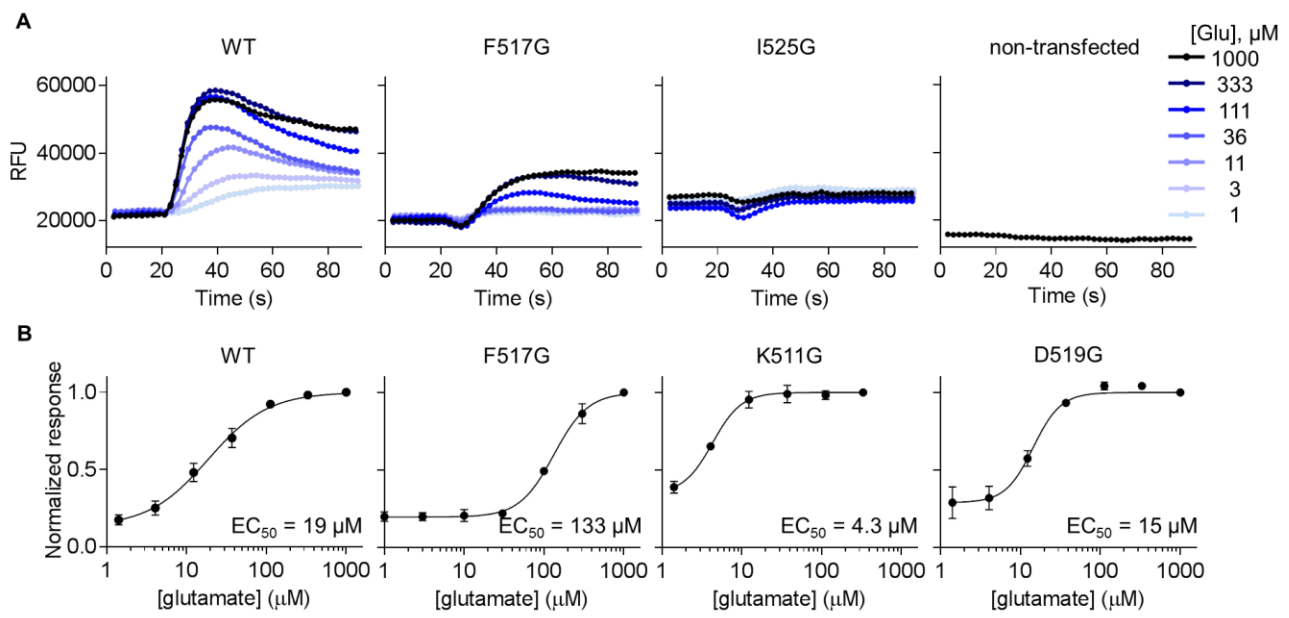
## 12. Figures

Figure 1



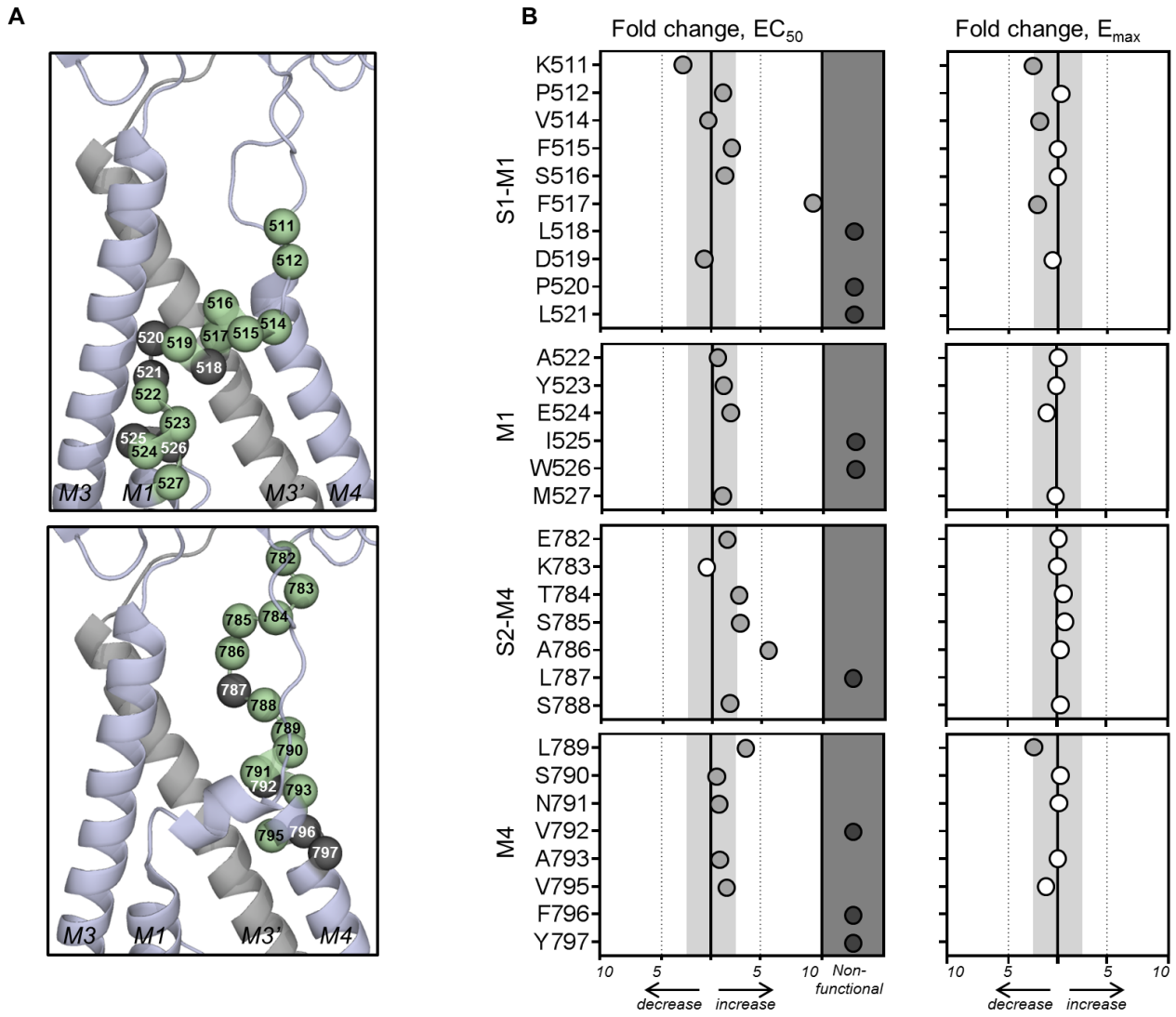
MOL # 116871

Figure 2



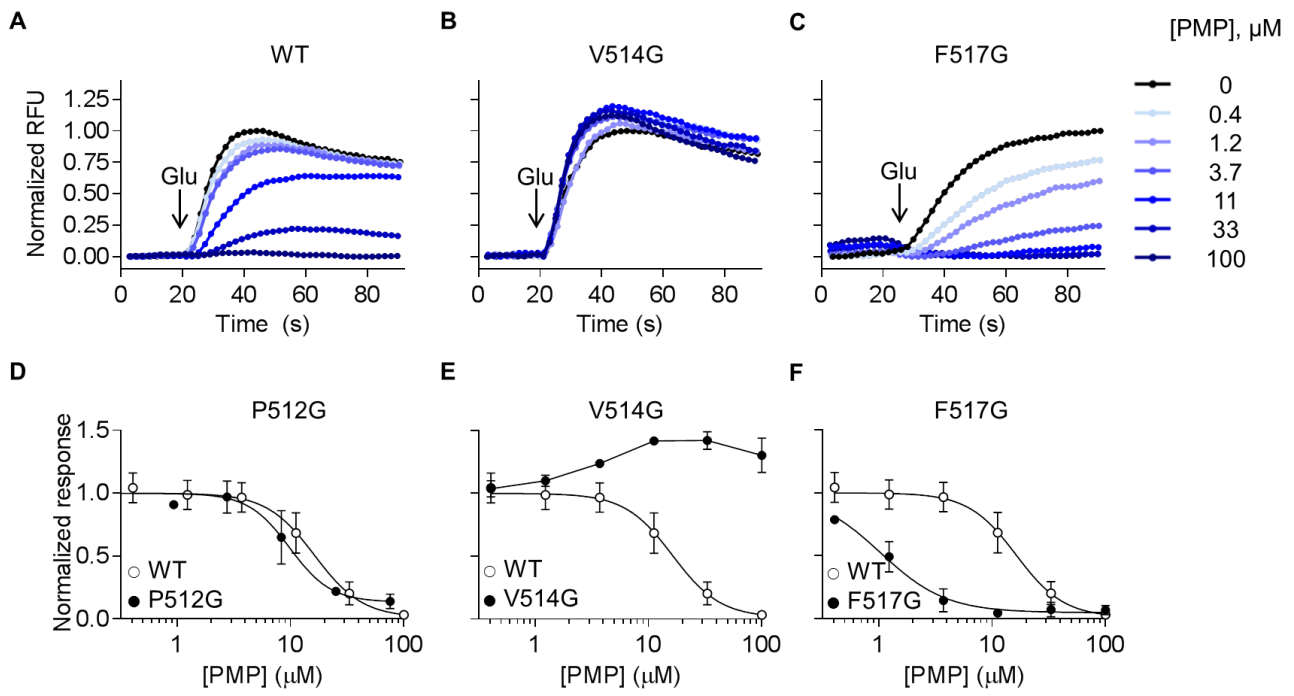
MOL # 116871

Figure 3



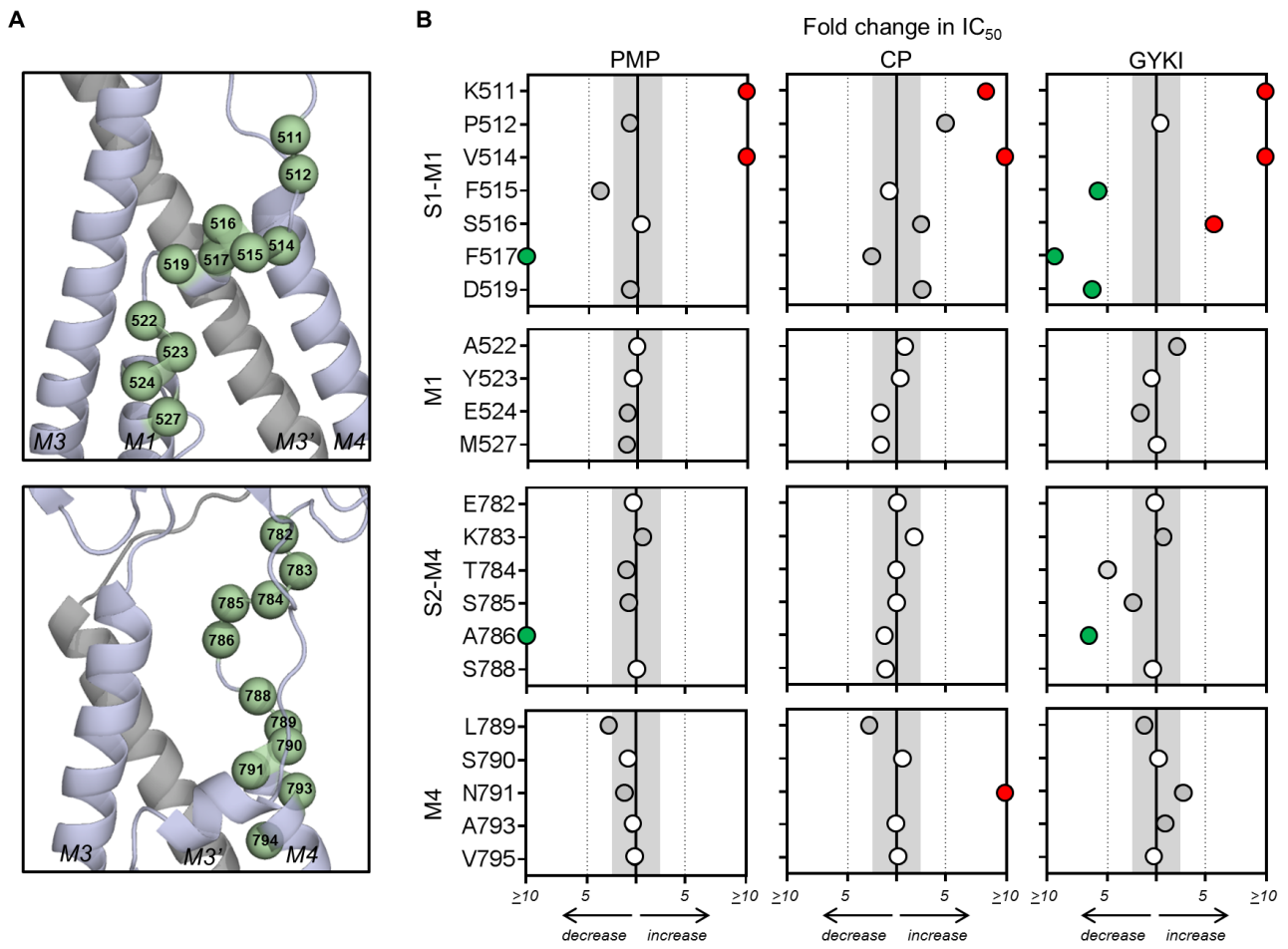
MOL # 116871

Figure 4



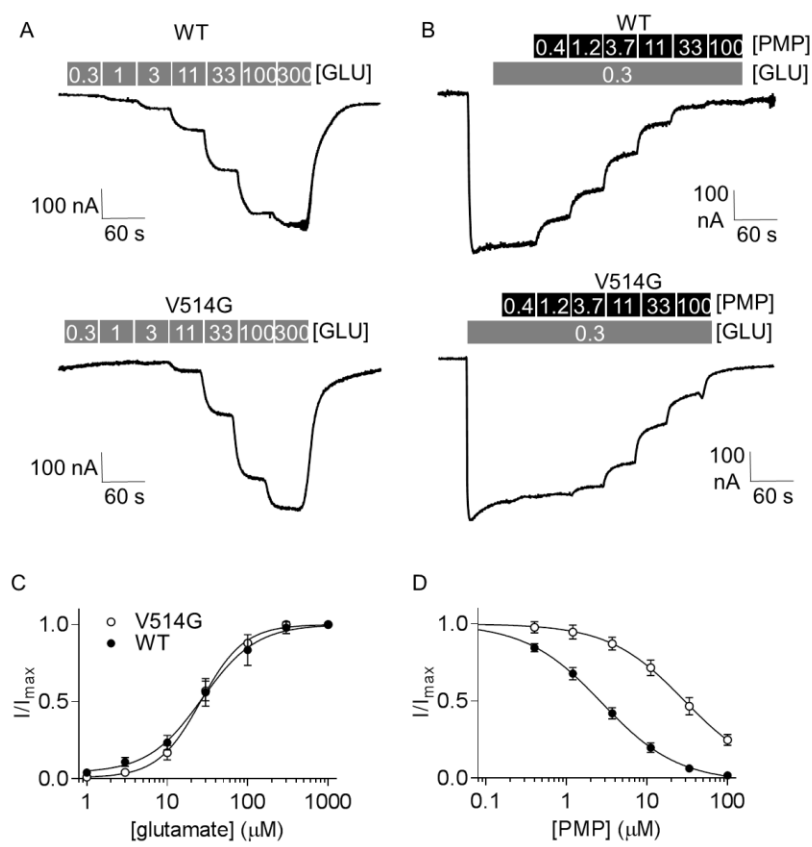
MOL # 116871

Figure 5



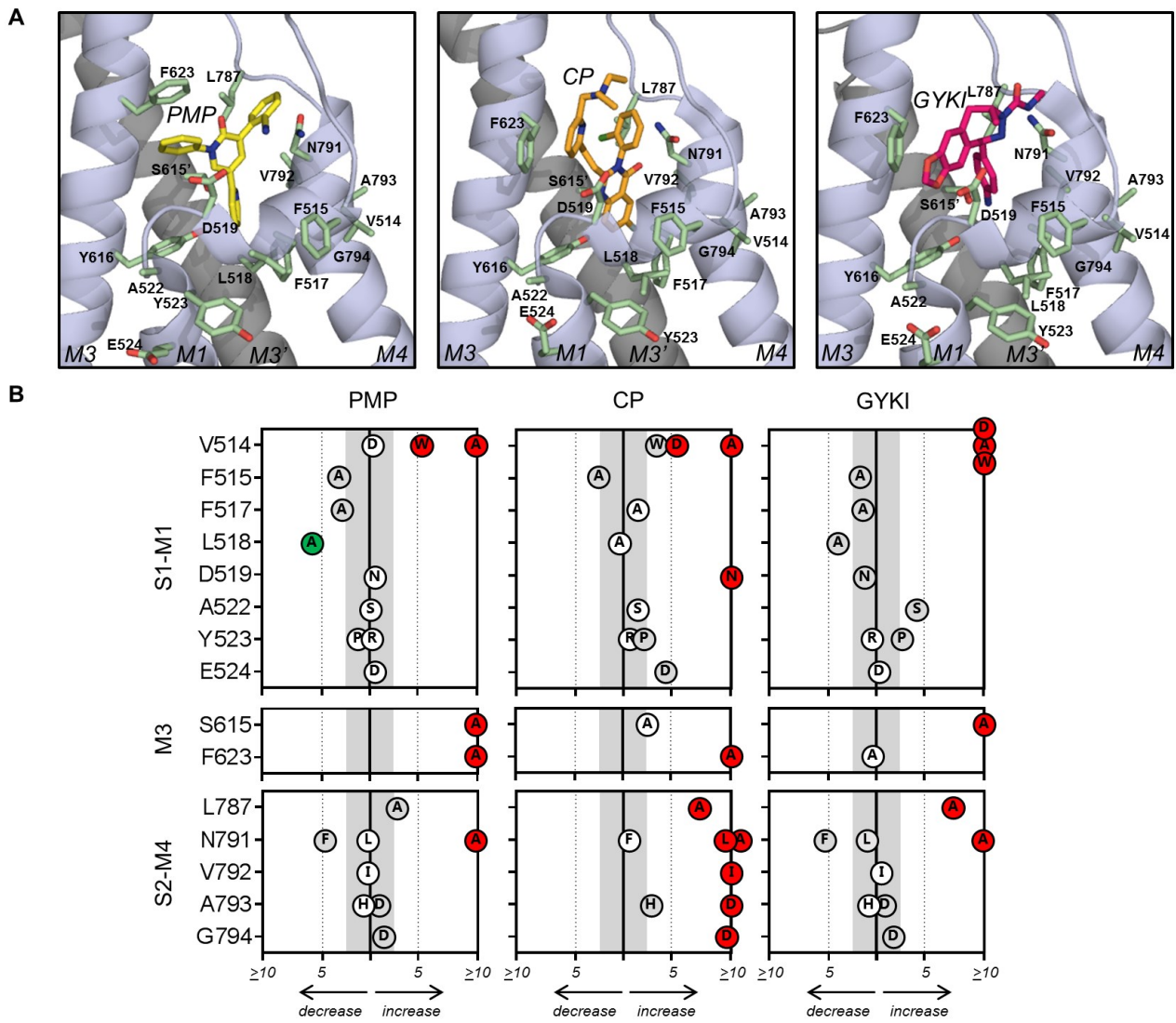
MOL # 116871

Figure 6



MOL # 116871

Figure 7





MOL # 116871

Figure 9

